Science Advances
AAAS

Supplementary Materials for

Programming angiogenesis with tunable assemblies of multifunctional peptides

Joseph Dodd-o *et al.*

Corresponding author: Vivek A. Kumar, vkumar24@cougarnet.uh.edu

Sci. Adv. **12**, eaef5064 (2026)
DOI: 10.1126/sciadv.aef5064

This PDF file includes:

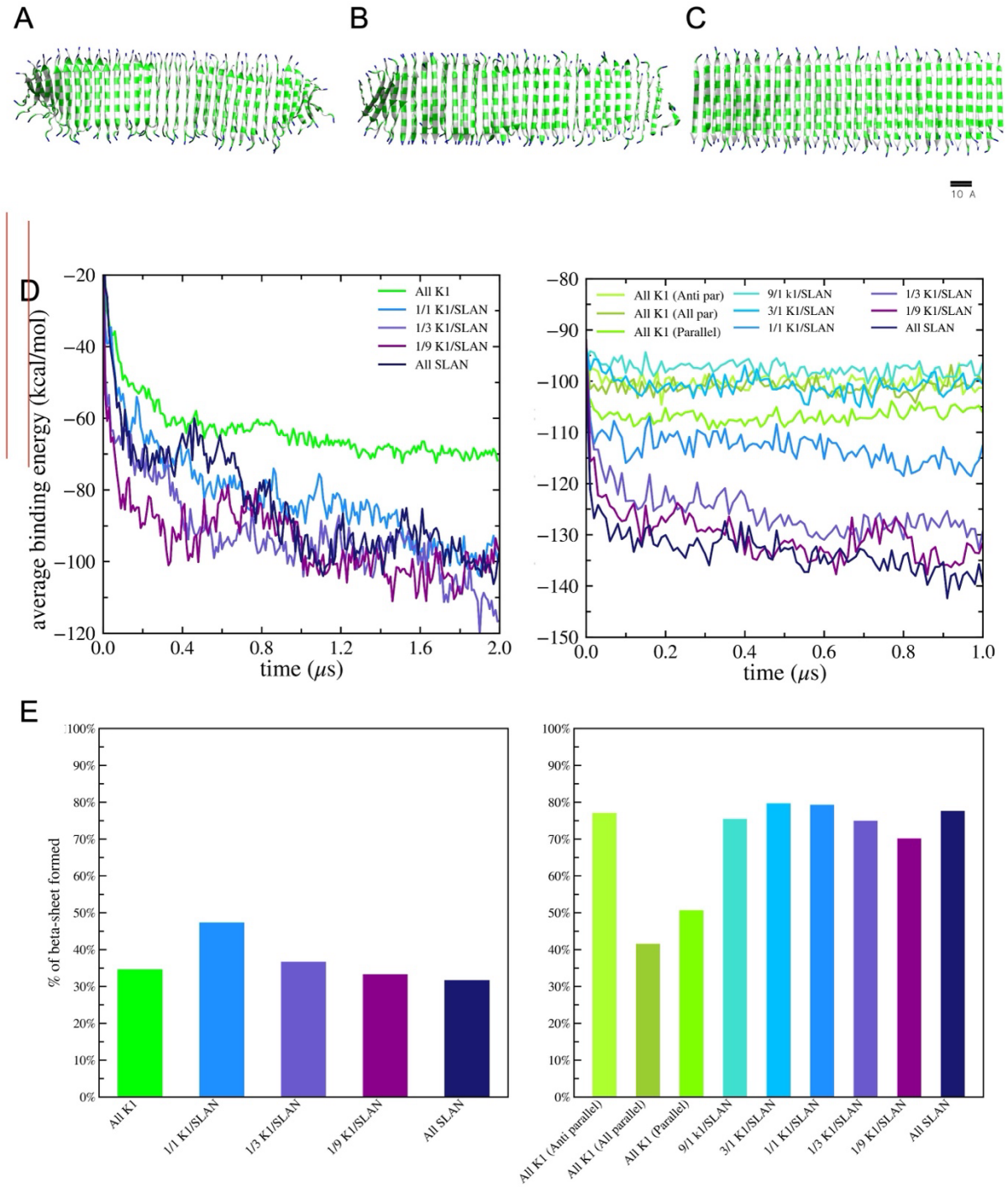

Figure S1. Fiber Assembly of Homogenous and Composite Angiogenic Hydrogels. MD investigations into combinations for improving epitope presentation. 400ns simulations interrogated the stability of base K1 in all parallel **(A)** planar antiparallel **(B)** and bidirectional antiparallel **(C)** configurations to determine the base self-assembling sequence K1's preferential arrangement. **(D)** Energy vs. time plots for (left) fibril nucleation studies and (right) preformed fibril studies. **(E)** % β-sheet of the K1, SLan and fibril assemblies. Scale bar: 10Å.

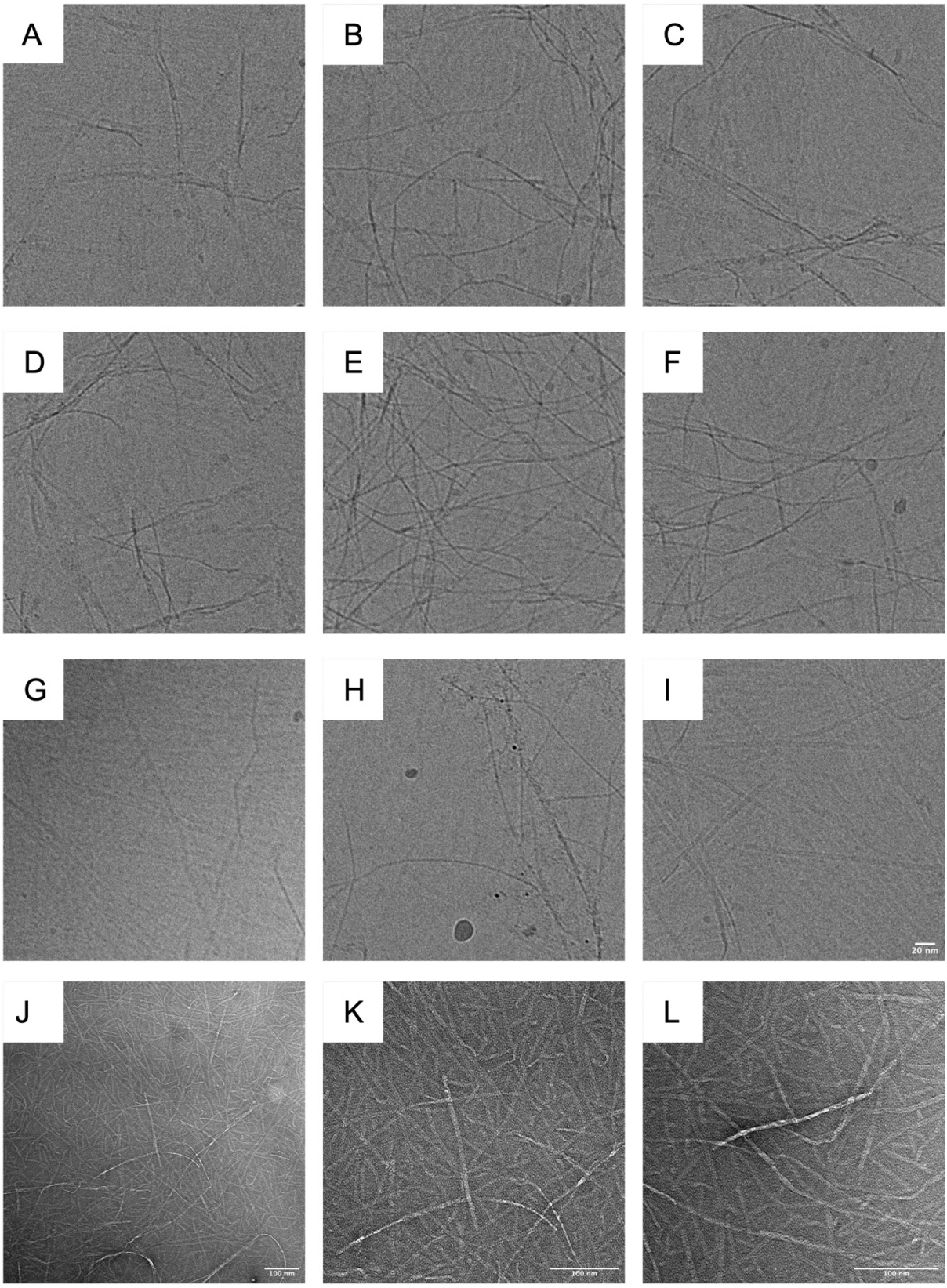

Figure S2. Additional electron microscopy images of K1. Various observed morphologies of K1 observed using Cryo-EM on **(A-F)** carbon grids and **(G-I)** gold grids. The formation of long, twisting fibrils

was also observed using negative stain TEM **(J)**, magnified in **(K)**, and a different region **(L)**. Scale bar - A-I: 20nm, J-L: 100nm. Fiber lengths of 15 measured fibers: 241 ± 42nm (mean ± sd).

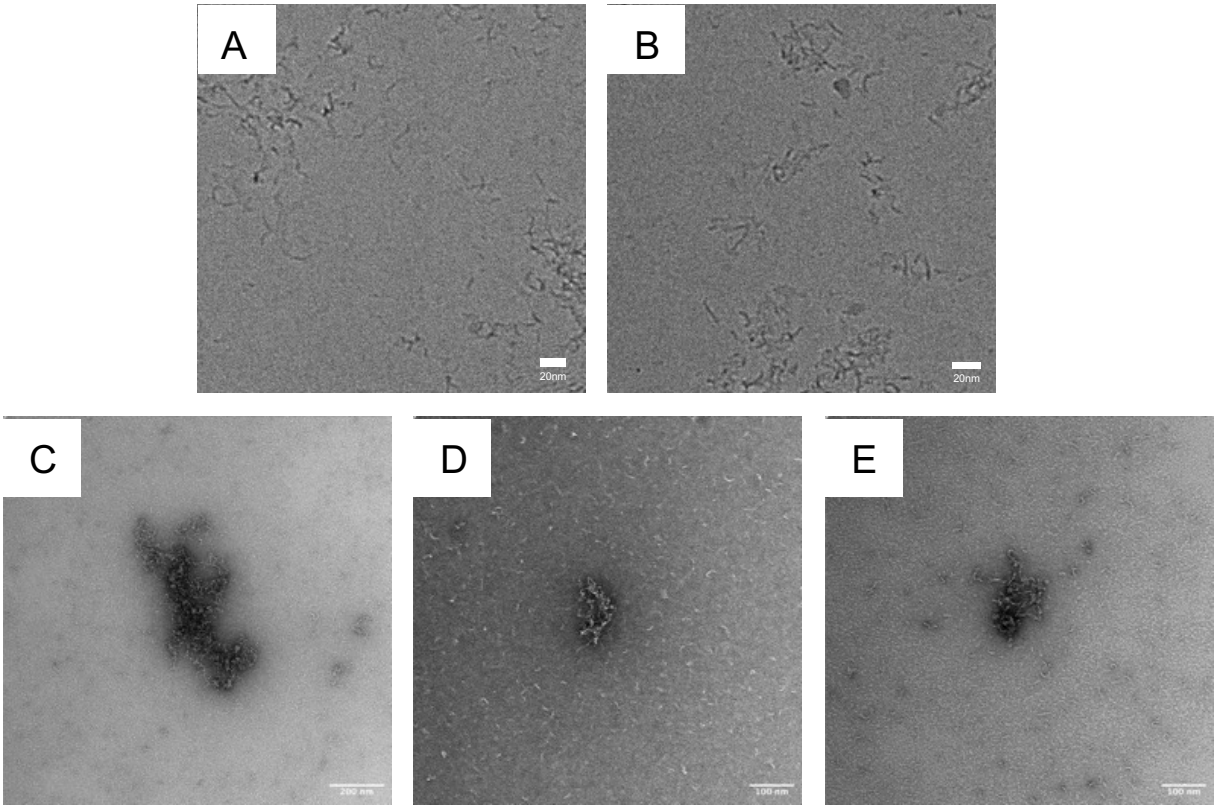

Figure S3. Additional electron microscopy images of SLan. Various observed morphologies of SLan observed using Cryo-EM on gold grids **(A-B)**. **(C-E)** Negative stain TEM images of SLan in solution with uranyl acetate as the negative stain. Scale bar - A-C: 20nm, D: 200nm, E-F: 100nm. Fiber lengths of 15 measured fibers: 30 ± 3.2nm (mean ± sd).

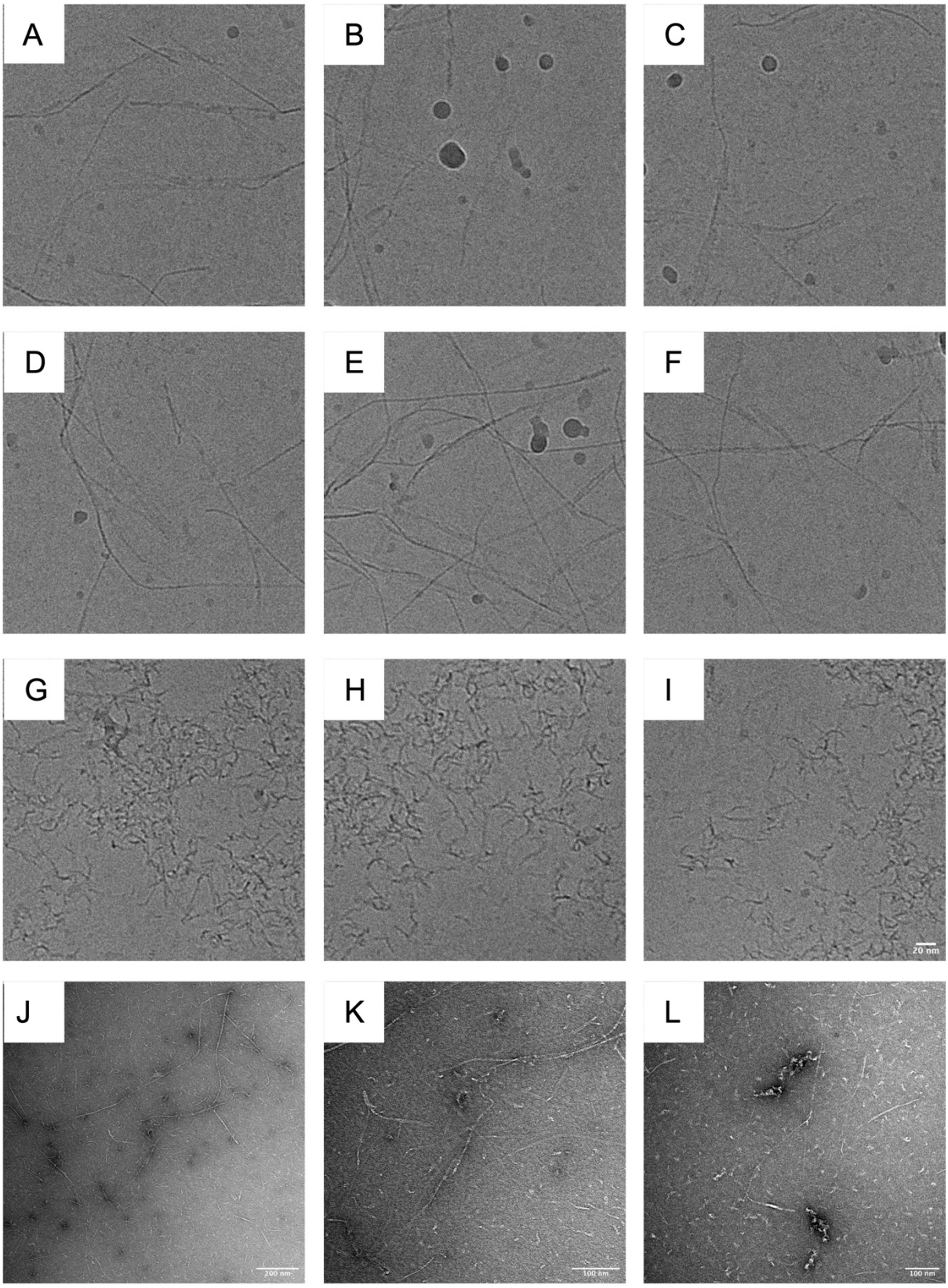

Figure S4. Additional electron microscopy images of 1:1 SLan:K1. Various observed morphologies of the 1:1 SLan:K1 combo. **(A-F)** We observed longer fibrils when imaging with Cryo-EM on vortexed

samples. The morphology is like in K1. **(G-I)** When agitated with a probe-type ultrasound sonicator, the fibrils become shorter and similar in morphology to SLan. Negative stain TEM images show heterogeneity in fibril length, but longer fibrils observed with K1 **(J)**, magnified in **(K)**, and a different region **(L)**. Scale bar - A-I: 20nm, J: 200nm, K-L: 100nm. Fiber lengths of 15 measured fibers: 225 ± 37nm (mean ± sd).

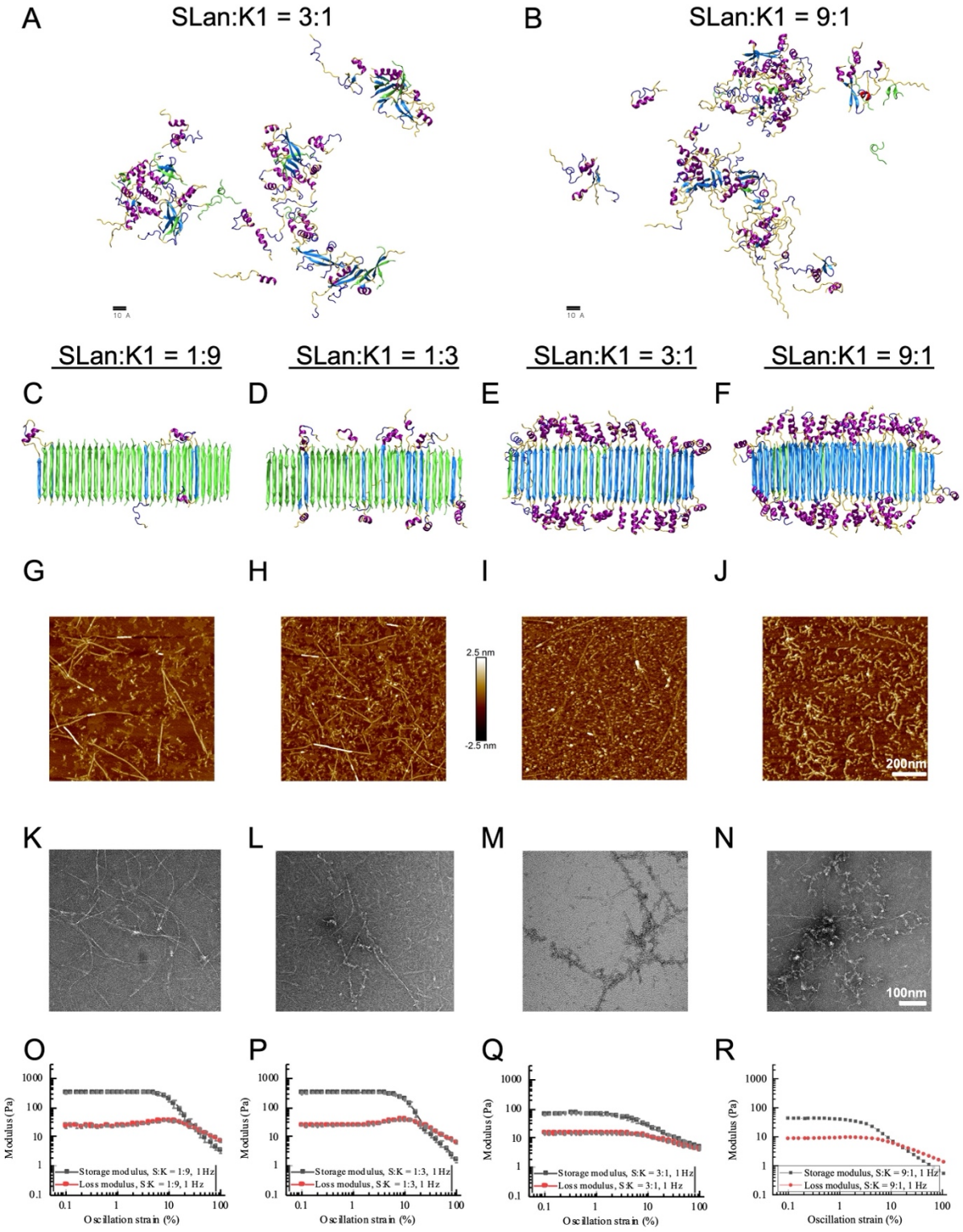

Figure S5. Fiber Assembly of Other Combination Hydrogels. (A) The α-helical bioactive domain (purple) of SLan interferes extensively with the nucleation of fibrils in 3:1 SLan:K1 fibrils, with the effect even more pronounced in **(B)** 9:1 SLan:K1. **(C-F)** Investigations into the stability of assembled 1:9, 1:3, 3:1, 9:1 SLan:K1 composite fibrils are consistent with homogenous assemblies, remaining energetically favorable conformations once assembled. **(G-J)** Atomic force microscopy investigations into fibrils deposited on mica disks show progressively smaller fibrils as the proportion of SLan increases (scale bar 200nm). **(K-N)** This observation was repeated with transmission electron microscopy images (scale bar: 100nm). **(O-R)** The pattern of shorter fibrils with more SLan was again corroborated by the composite hydrogel's bulk mechanical properties. The magnitude of low strain storage modulus (black line, left of the sloped region) decreases with increasing SLan combination.

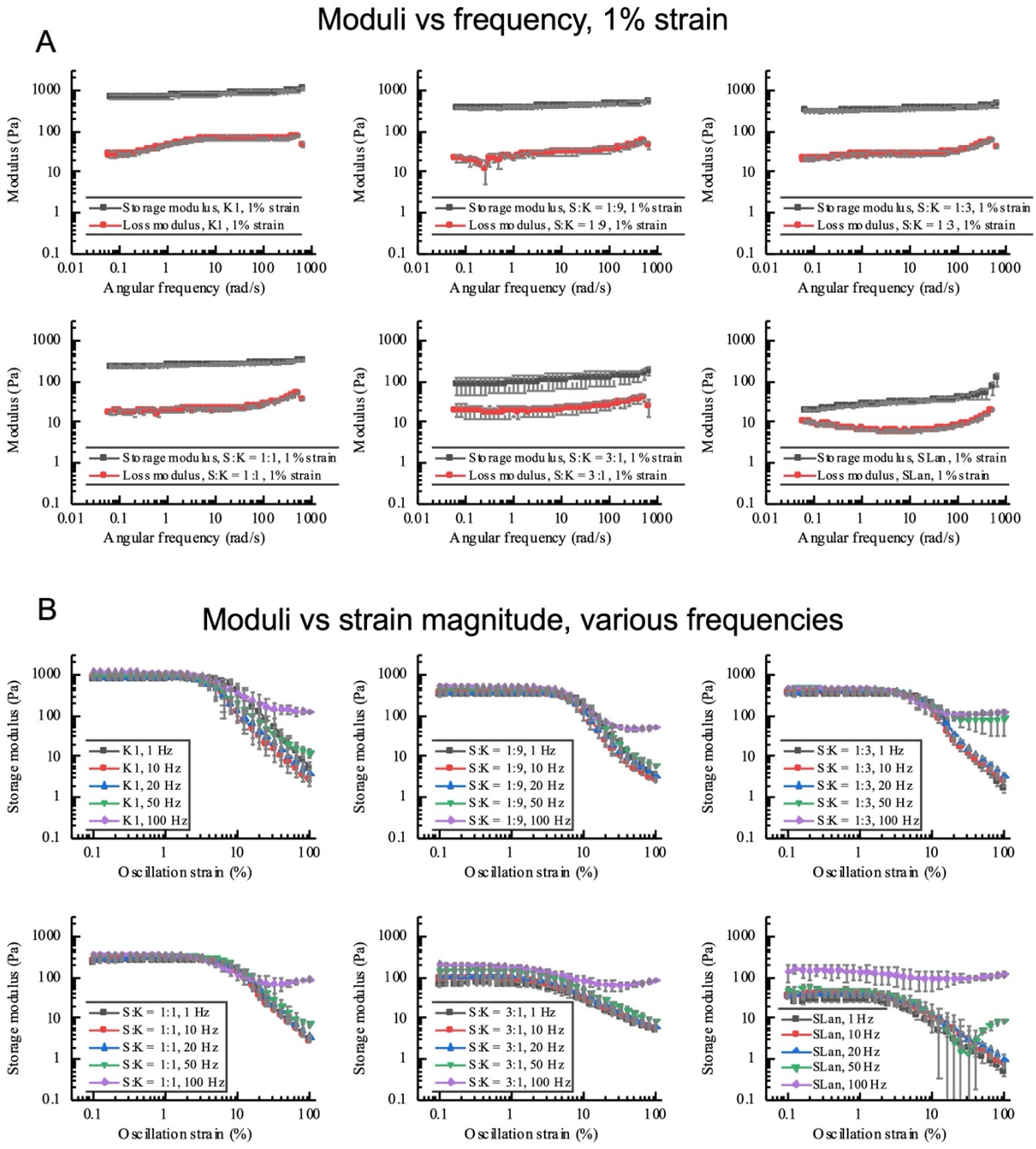

Figure S6. Effect of different strain regimes on bulk mechanical properties. (A) Frequency sweep at 1% strain interrogates the assembly's viscoelastic properties under a low strain regime, determining if increasing the strain frequency can upset the overall structure. We found the storage and loss modulus values to match closely with our strain sweep values at low strain magnitudes, and that increasing the frequency does not upset the overall structure, a feature largely conserved across the combination hydrogels. Storage and loss moduli, along with strain magnitude and SLan:K1 ratios (shorthanded as S:K) are found in each plot's legend. **(B)** Storage modulus values at high strain rates remained higher at high frequencies vs low frequencies. SLan:K1 ratios (shorthanded as S:K) and oscillation frequency are noted in the plot legends

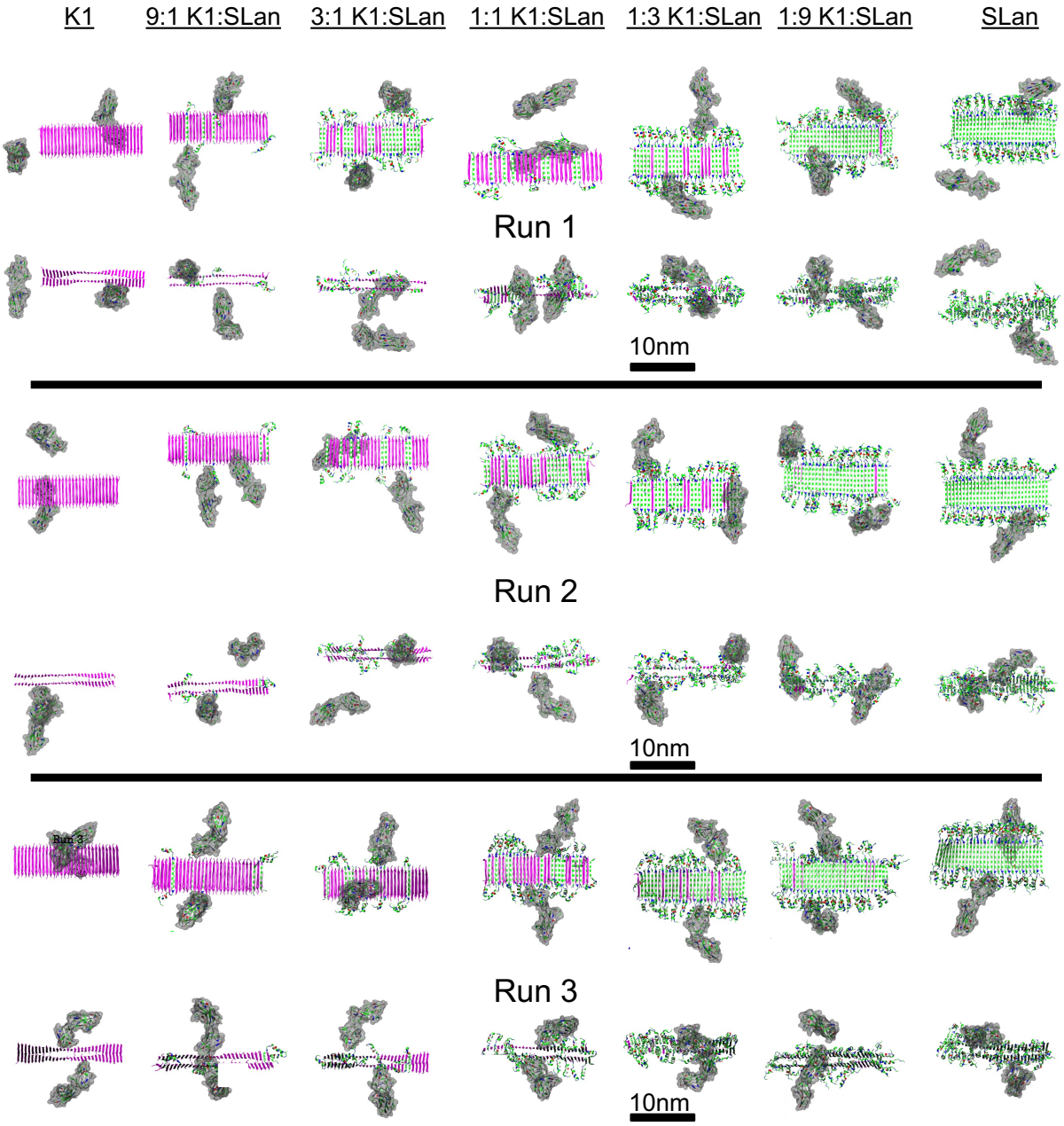

Figure S7. Interactions of Fiber Assemblies with VEGFR2. Above fiber and between fiber leaflet views of the experimental setup for runs 1 – 3. Each run had 2 VEGFR2 D2-3 models at different points along the fibril (n=6). Representations of K1 monomers are in pink, SLan in green, and VEGFR2 in gray.

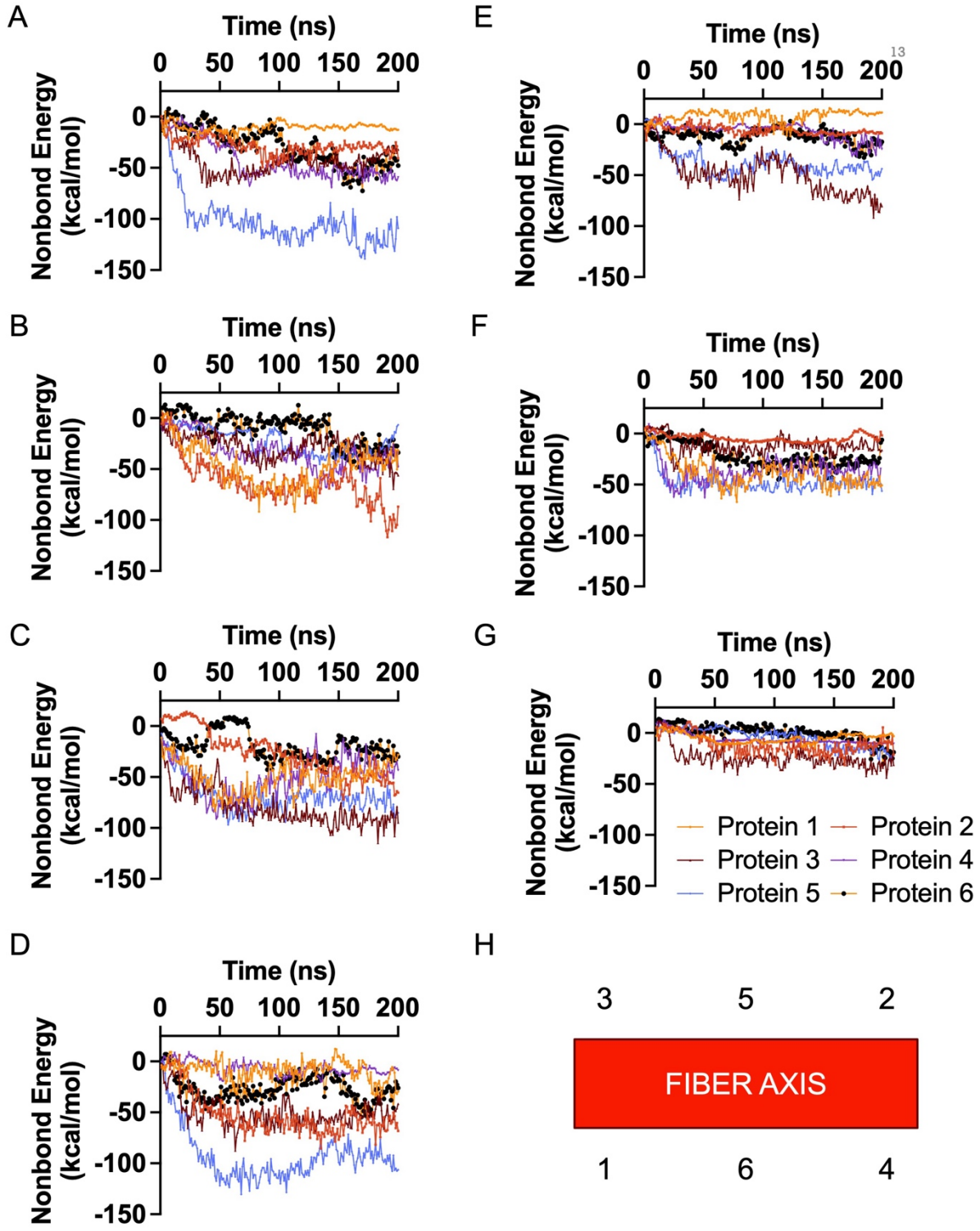

Figure S8. Energy vs. Time Plots of Combination Fibers against VEGFR2. Binding Energy vs. Time for plots for 6 trajectories of **(A)** SLan, **(B)** 9:1 SLan:K1, **(C)** 3:1 SLan:K1, **(D)** 1:1 SLan:K1, **(E)** 1:3 SLan:K1, **(F)** 1:9 SLan:K1, and **(G)** K1. (H) Diagram for the approximate starting positions for each representation of model VEGFR2 Domains 2-3 for the simulations.

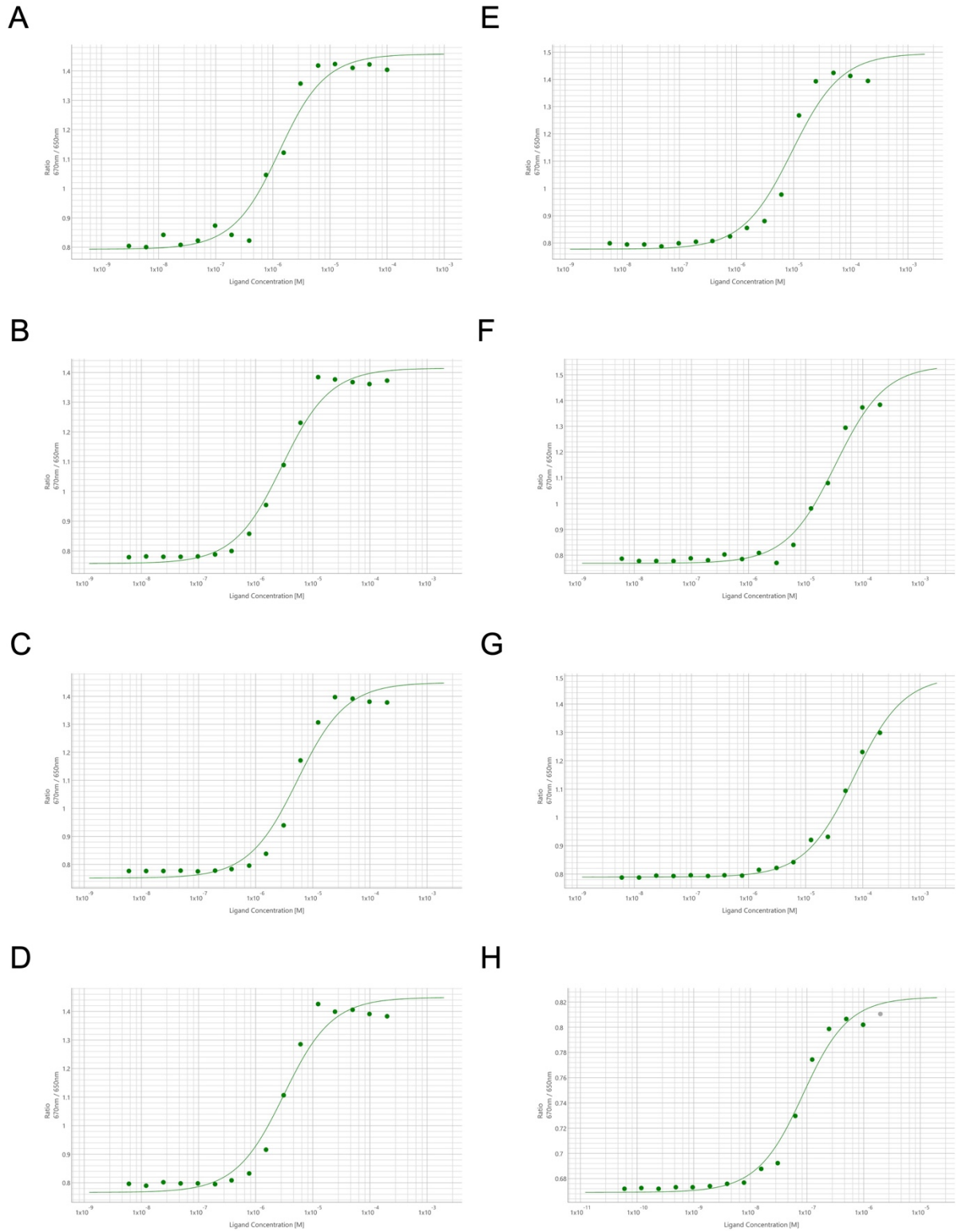

Figure S9. Raw Spectral Shift Plots. 670/650nm emission ratios at a constant time after laser initiation for :**(A)** SLan, **(B)** 9:1 SLan:K1, **(C)** 3:1 SLan:K1, **(D)** 1:1 SLan:K1, **(E)** 1:3 SLan:K1, **(F)** 1:9 SLan:K1, and **(G)** K1. **(H)** His-tag receptor / Tris-NTA dye conjugate binding kinetics curve.

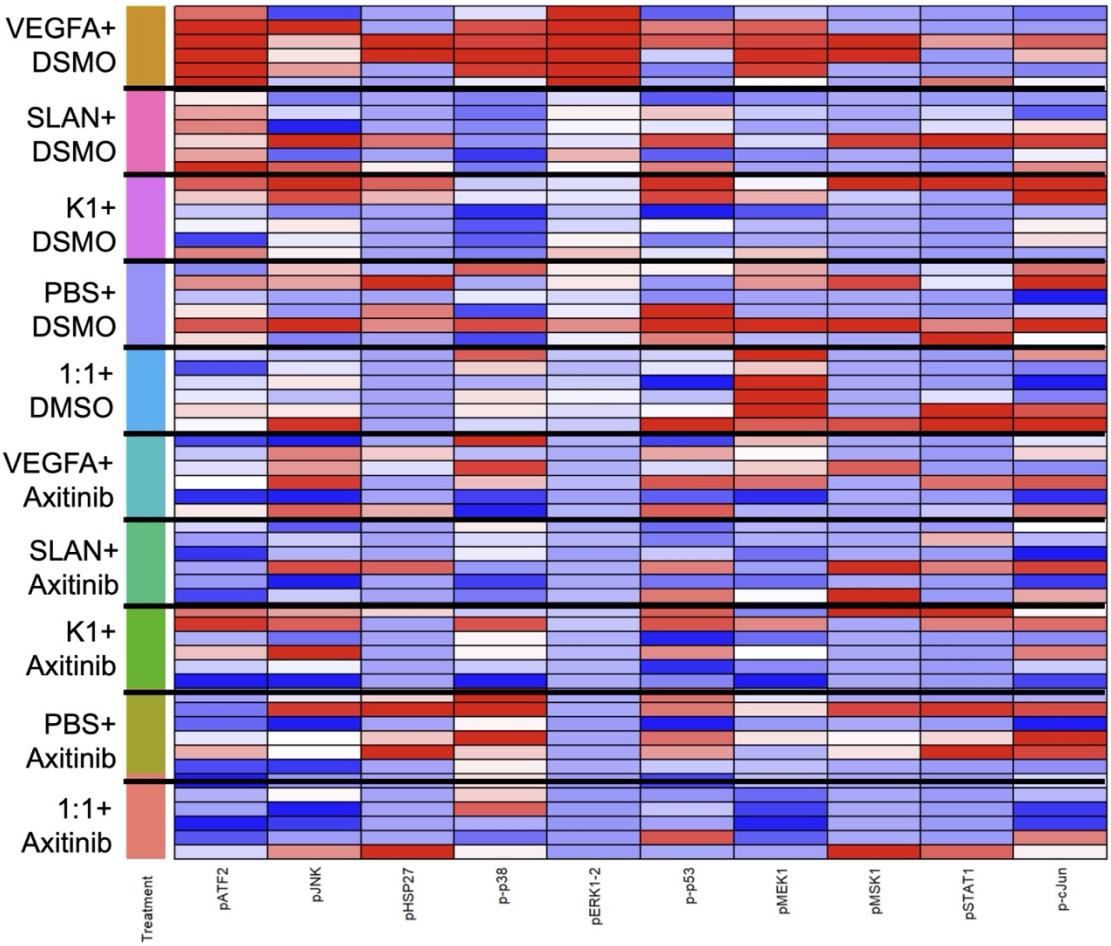

Figure S10. MAPK 11-Plex Luminex reading heat map. Phosphoprotein analysis for HUVEC lysate stimulated with various combinations, with background subtracted.

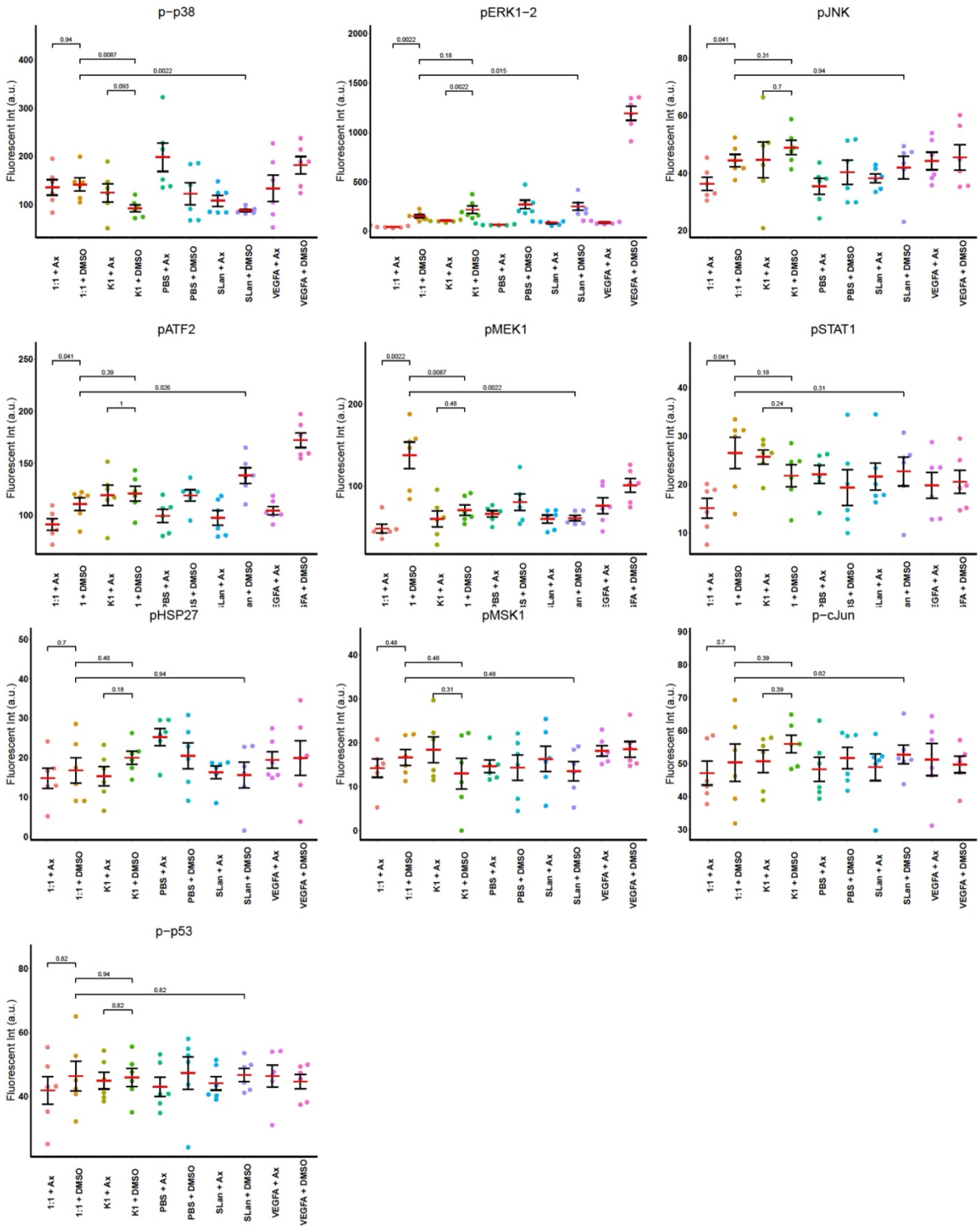

Figure S11. MAPK 11-Plex Luminex reading background corrected values. Phosphoprotein analysis for HUVEC lysate stimulated with various combinations, without background subtracted. Data represented as mean +/- SEM. Data is plotted as mean +/- SEM, and p-values between groups were calculated using a Wilcoxon rank-sum test with a Bonferroni correction applied for multiple comparisons.

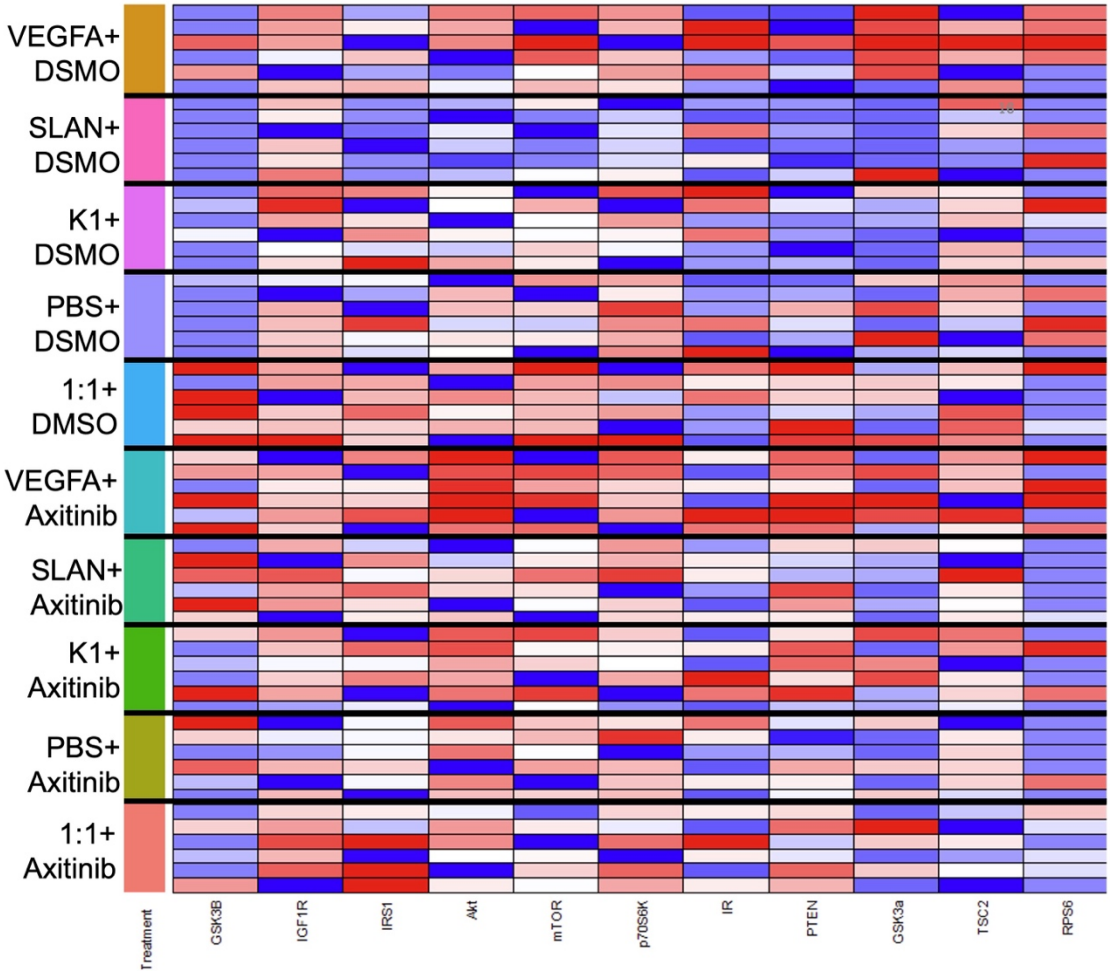

Figure S12. AKT 11-Plex Luminex reading heat map. Phosphoprotein analysis for HUVEC lysate stimulated with various combinations, with background subtracted.

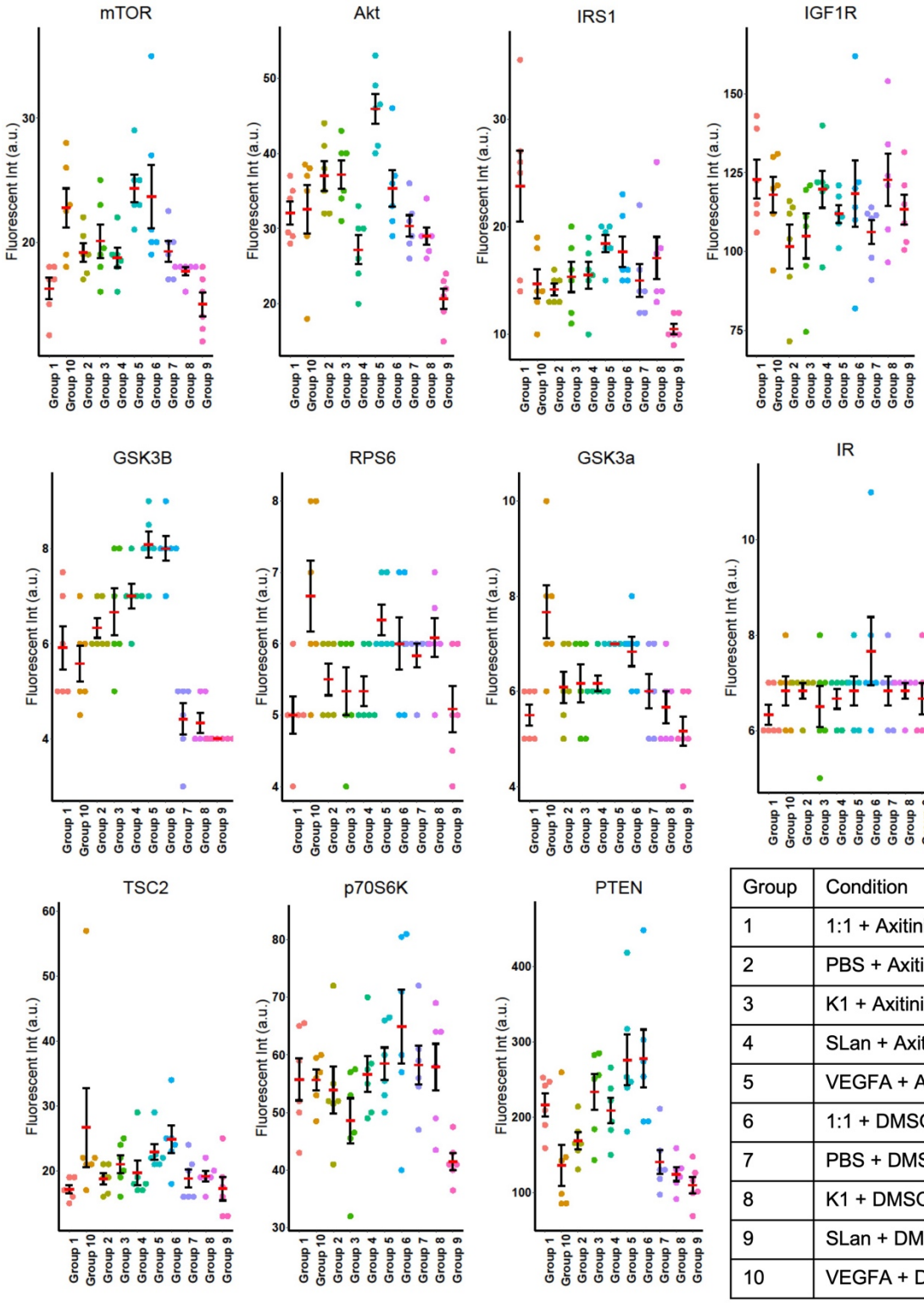

Group	Condition
1	1:1 + Axitinib
2	PBS + Axitinib
3	K1 + Axitinib
4	SLan + Axitinib
5	VEGFA + Axitinib
6	1:1 + DMSO
7	PBS + DMSO
8	K1 + DMSO
9	SLan + DMSO
10	VEGFA + DMSO

Figure S13. AKT 11-Plex Luminex reading background corrected values. Phosphoprotein analysis for HUVEC lysate stimulated with various combinations, without background subtracted. Results are blinded groups; the key for groups is at the bottom right. Data is plotted as mean +/- SEM, and p-values between groups were calculated using a Wilcoxon rank-sum test with a Bonferroni correction applied for multiple comparisons.

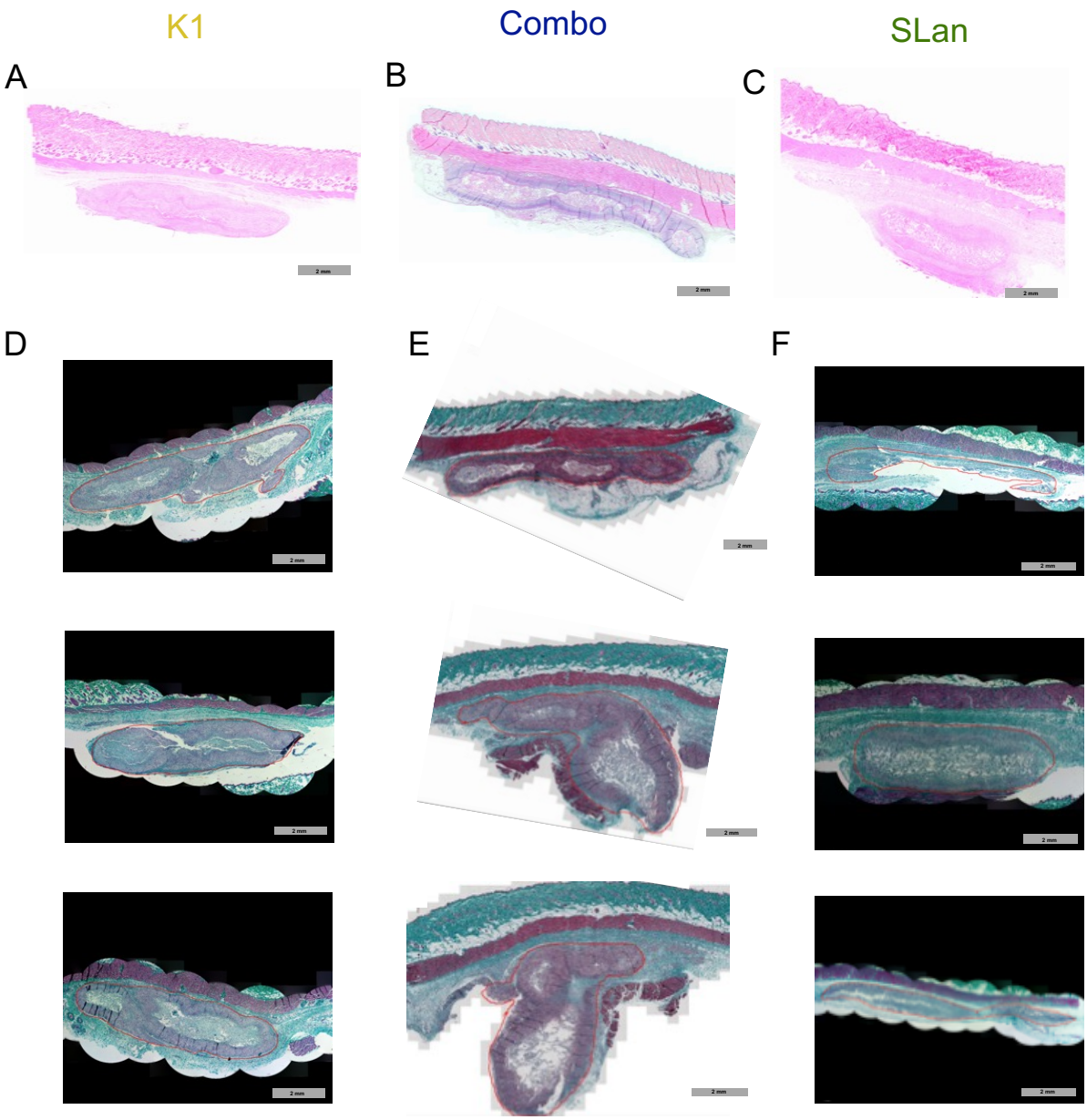

Figure S14. Vessel quantification, MT images, H&E images of subcutaneous bolus injections. Example H&E stained explant slices for **(A)** K1, **(B)** 1:1 SLan:K1, **(C)** K1 boluses 7 days following a 200µL subcutaneous injection into a rat. **(D)** Masson's trichrome stained bolus images for K1 used for bolus vessel density quantification, with the bolus highlighted. **(E)** MT stained slide images for the 1:1 SLan:K1 combination, with the bolus highlighted. **(F)** Images for MT stained explants of SLan. Scale bar: 2mm.

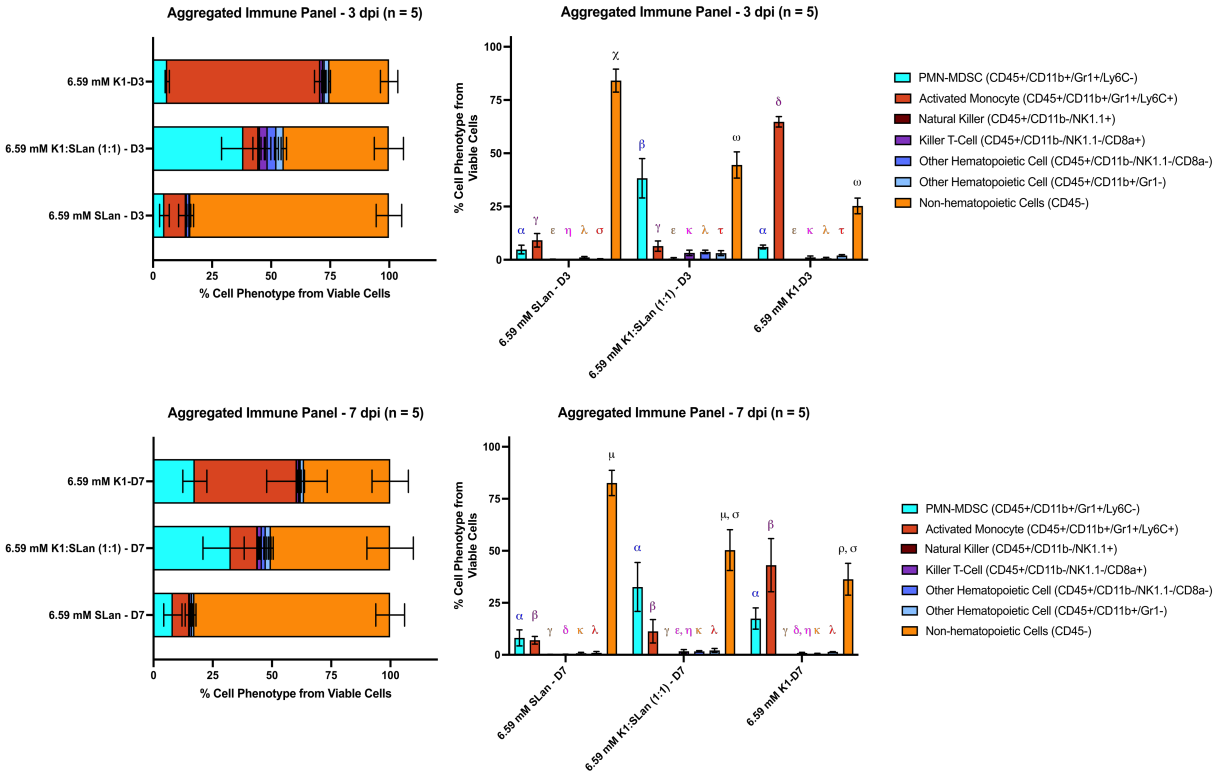

Figure S15. Immune Marker Infiltrates analysis. Fluorescence activated cell sorting used to show mean infiltration of Gr-1+/LY6C- myeloid cell (CD45+/CD11b+/Gr-1+/Ly6C-), Activated Monocytes (CD45+/CD11b+/Gr-1+/Ly6C+), Natural Killer (CD45+/CD11b-/NK1.1+), Killer T-Cell (CD45+/CD11b-/NK1.1-/CD8a+), Other Hematopoietic Cell (CD45+/CD11b-/NK1.1-/CD8a-), Other Hematopoietic Cell (CD45+/CD11b+/Gr-1-), and Non-Hematopoietic (CD45-) cells three (top row) and seven (bottom row) days post injection from the Viable Cells; error bars represent SEM. Significance between groups is represented by Greek letters where different letters indicate a significant difference & instances where the same symbol is present means no significant difference is observed. Statistical analysis performed in RStudio 4.3.1.

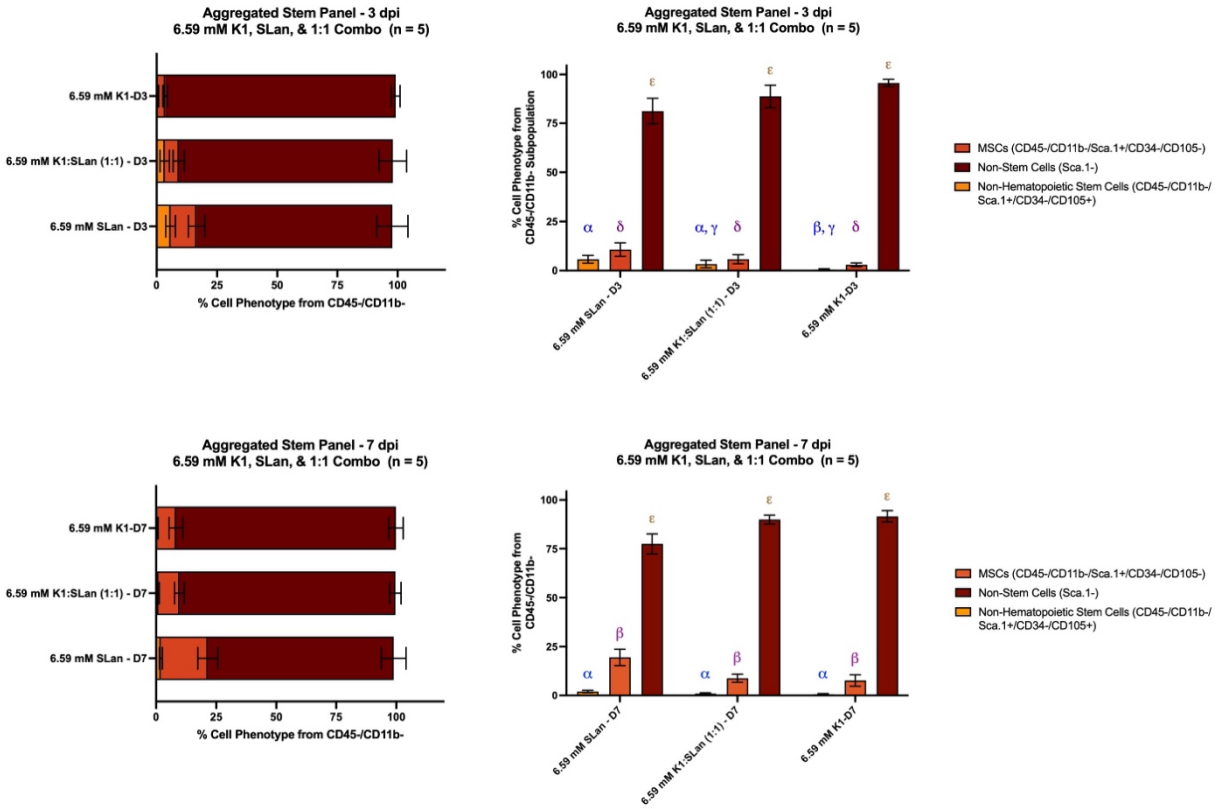

Figure S16. Aggregated Stem Cell Marker Infiltrates analysis. Fluorescence activated cell sorting used to show mean infiltration of Mesenchymal Stem Cells (CD45-/CD11b-/Sca-1+/CD34-/CD105-), Non-Stem Cells (Sca-1-), and Non-Hematopoietic Stem Cells (CD45-/CD11b-/Sca-1+/CD34-/CD105+) from three (top row) and seven (bottom row) days post injection from the CD45-/CD11b- Subpopulation; error bars represent SEM. Significance between groups is represented by Greek letters where different letters indicate a significant difference & instances where the same symbol is present means no significant difference is observed. Statistical analysis performed in RStudio 4.3.1.

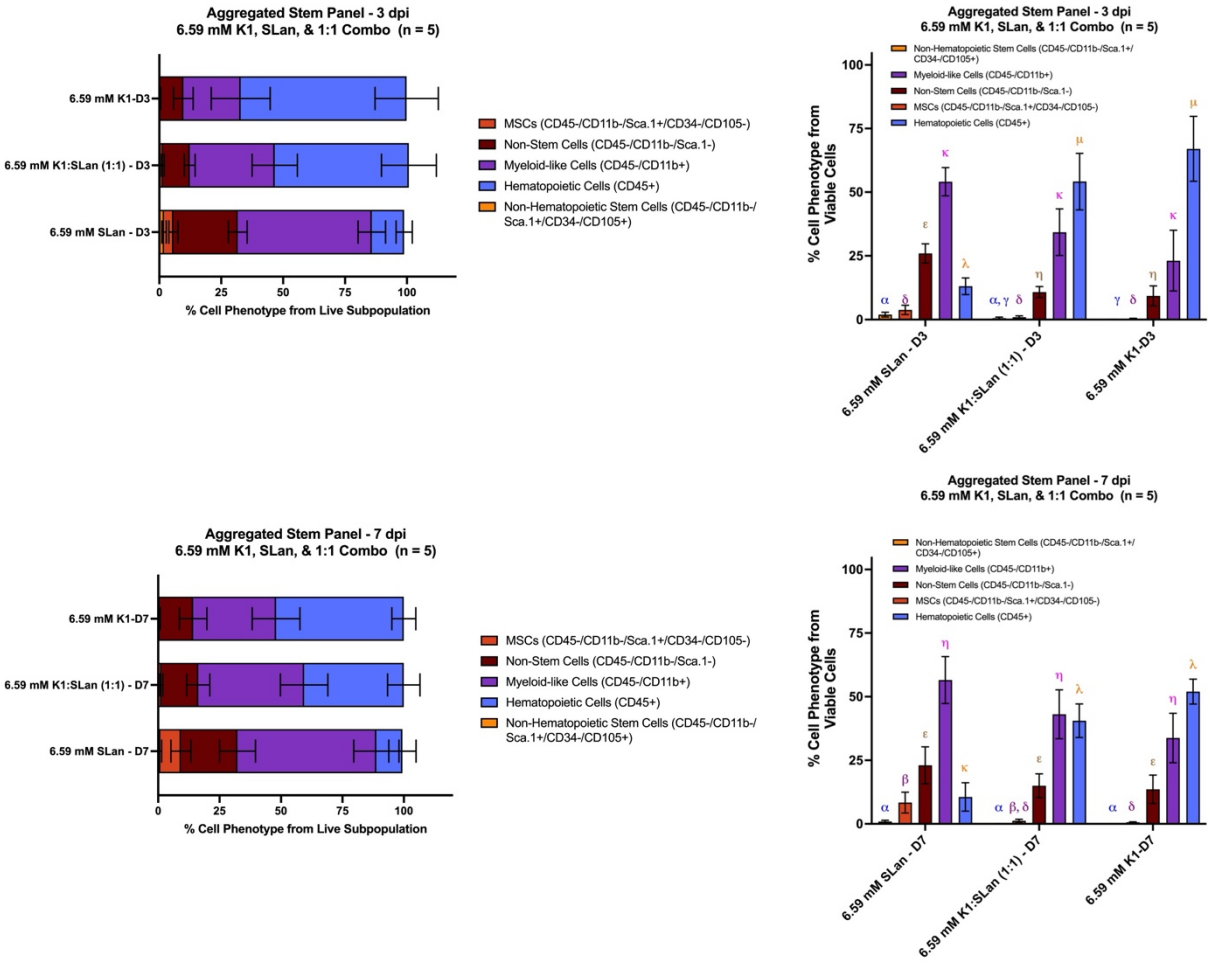

Figure S17. Separated Stem Cell Marker Infiltrates analysis. Fluorescence activated cell sorting used to show mean infiltration of Mesenchymal Stem Cells (CD45-/CD11b-/Sca-1+/CD34-/CD105-), Non-Stem Cells (Sca-1-), Non-Hematopoietic Stem Cells (CD45-/CD11b-/Sca-1+/CD34-/CD105+), Myeloid-like Cells (CD45-/CD11b+), and Non-Stem Cells (CD45-/CD11b-/Sca-1-) from three (top row) and seven (bottom row) days post injection from the Live Cells; error bars represent SEM. Significance between groups is represented by Greek letters where different letters indicate a significant difference & instances where the same symbol is present means no significant difference is observed. Statistical analysis performed in RStudio 4.3.1.

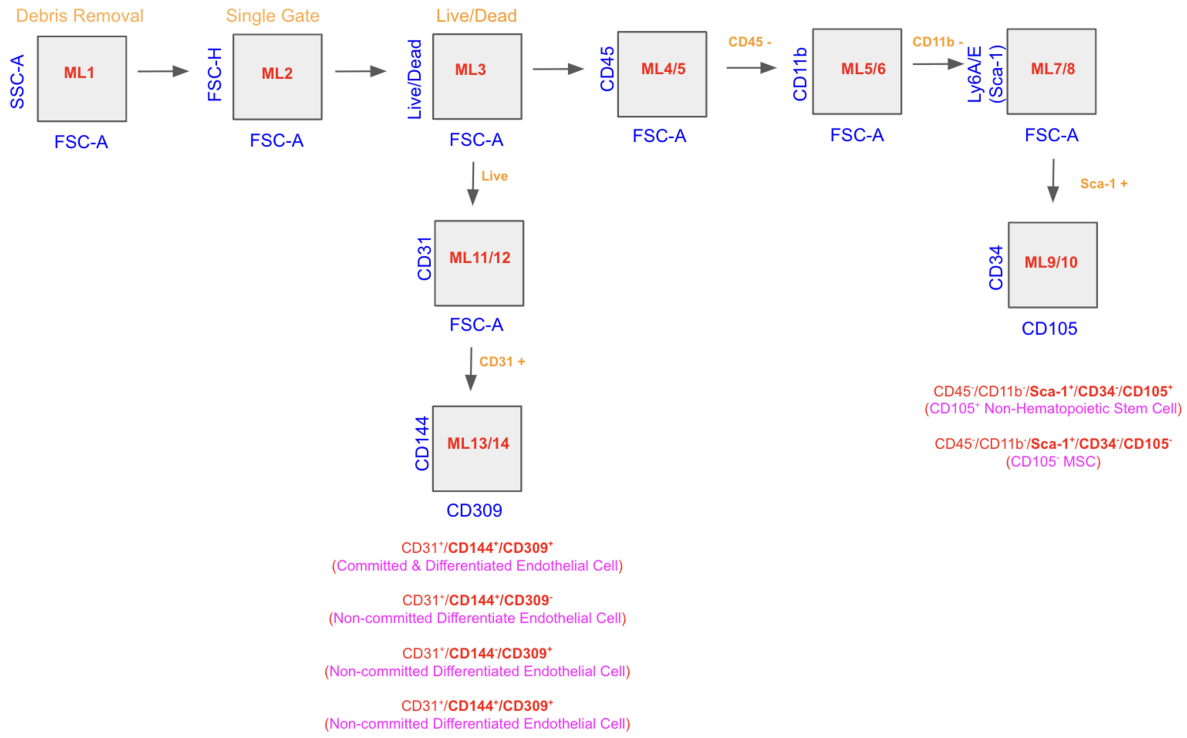

Figure S18. Fluorescence activated cell sorting gating strategy - Endothelial & Stem Cell Panel

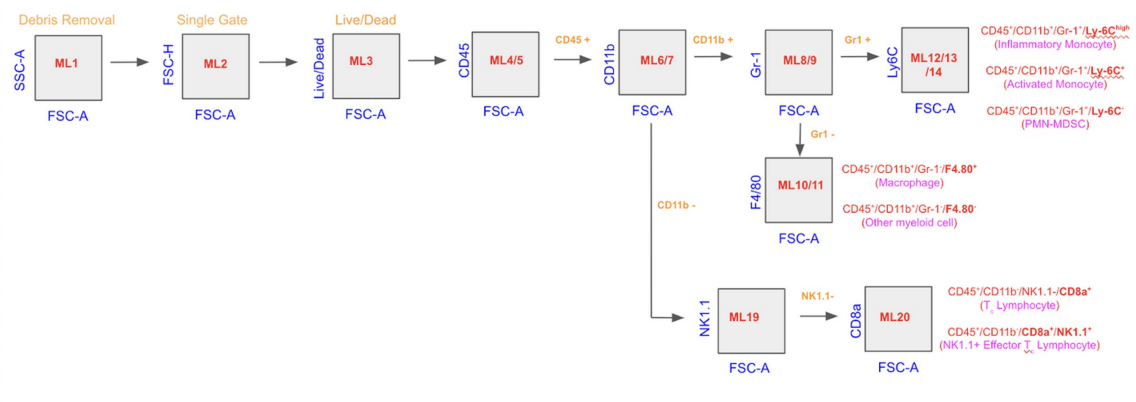

Figure S19. Fluorescence activated cell sorting gating strategy - Hematopoietic and Immune Cell Panel.

Stem Cell & Angiogenesis Panel - Murine Subcutaneous Tissue Explant:				
Marker:	**Catalog #:**	**Fluorophore:**	**Laser:**	**Filter:**
CD45	BD Biosciences, 561037	APC-Cyanine 7	Red (R3)	780/60
CD309 (FLK1/VEGFR2)	Invitrogen, 62-5821-82	SuperBright 436	Violet (V1)	450/40
CD144 (VE-Cadherin)	Invitrogen, 63-1441-82	SuperBright 600	Violet (V3)	610/20
CD31 (PECAM-1)	Invitrogen, 15-0311-82	PE-Cyanine5	Yellow (Y3)	670/14
CD105 (Endoglin)	BD Biosciences, 562761	Alexa Fluor 647	Red (R1)	660/20
Ly-6A/E (Sca-1)	Invitrogen, 407-5981-82	Brilliant Violet 711	Violet (V5)	710/50
CD34	Invitrogen, MA517831	PE	Yellow (Y1)	590/20
CD11b	BD Biosciences, 561686	FITC	Blue (B1)	530/30
Live/Dead Blue	Invitrogen, L23105		UV (355 nm) U2-5/7	450/50

Table S1. Fluorescence activated cell sorting marker selection - Endothelial/Stem Cell Panel.

Myeloid & Lymphoid Panel - Murine Subcutaneous Tissue Explant:				
Marker:	**Supplier & Catalog #:**	**Fluorophore:**	**Laser:**	**Filter:**
CD45	BD Biosciences, 561037	APC-Cyanine 7	Red (R3)	780/60
Gr-1 (Ly-6G/Ly-6C)	Invitrogen, 64-5931-82	SuperBright 645	Violet (V4)	670/30
Ly-6C	BD Biosciences, 560593	PE-Cyanine 7	Yellow (Y5)	780/60
CD11b	BD Biosciences, 561686	FITC	Blue (B1)	530/30
F4/80	Invitrogen, 363-4801-80	Brilliant Ultraviolet 395	UV (U1)	379/28
NK1.1	Invitrogen, 78-5941-82	SuperBright 780	Violet (V6)	780/60
CD8a	Invitrogen, 563046	Brilliant Violet 711	Violet (V5)	710/50
Live/Dead Blue	Invitrogen, L23105		UV (355 nm) U2-5/7	450/50

Table S2. Fluorescence activated cell sorting marker selection – Hematopoeitic and Immune Cell Panel.

Supplier & Catalog #:	Antigen:	Conjugate:	Clone:	Quantity:	Species Reactivity:	Host Specie/Isotype:
Invitrogen, 63-1441-82	CD144 (VE-Cadherin)	SuperBright 600	eBioBV13 (BV13)	100 ug	Mouse	Rat/IgG1, kappa
Invitrogen, MA517831	CD34	PE	MEC14.7	50 ug	Mouse	Rat/IgG2a
Invitrogen, 15-0311-82	CD31 (PECAM-1)	PE-Cyanine5	390	100 ug	Mouse	Rat/IgG2a, kappa
Invitrogen, 367-0193-82	CD19	Brilliant UV 737	eBio1D3 (1D3)	100 ug	Mouse	Rat/IgG2a, kappa
Invitrogen, 64-5931-82	Ly-6G/Ly-6C	SuperBright 645	RB6-8C5	100 ug	Mouse	Rat/IgG2b, kappa
Invitrogen, 407-5981-82	Ly-6A/E (Sca-1)	Brilliant Violet 711	D7	100 ug	Mouse	Rat/IgG2a, kappa
Invitrogen, 78-5941-82	NK1.1	SuperBright 780	PK136	100 ug	Mouse	Mouse/IgG2a, kappa
Invitrogen, 363-4801-80	F4/80	Brilliant UV 395	BM8	25 ug	Mouse	Rat/IgG2a, kappa
Invitrogen, 62-5821-82	CD309 (FLK1/VEGFR 2)	SuperBright 436	Avas12a1	100 ug	Mouse	Rat/IgG2a, kappa
BD Biosciences, 561037	CD45	APC-Cyanine 7	30-F11	25 ug	Mouse	Rat Louvain (LOU)/C, LOU/M, IgG2b, kappa
BD Biosciences, 562761	CD105 (Endoglin)	Alexa Fluor 647	MJ7/18	50 ug	Mouse	Rat/IgG2a, kappa
BD Biosciences, 563046	CD8a	Brilliant Violet 711	53-6.7	50 ug	Mouse	Rat Louvain (LOU)/C, LOU/M, IgG2a, kappa
BD Biosciences, 561686	CD11b	FITC	M1/70	25 ug	Mouse	Mouse/IgG1, kappa
BD Biosciences, 560593	Ly-6C	PE-Cyanine 7	AL-21	50 ug	Mouse	Rat/IgM, kappa
BD Biosciences, 553141	Fc CD16/32		2.4G2	100 ug	Mouse	Rat SD/IgG2b, kappa

Table S3. Catalog of Flow Cytometry Labeling Reagents. Supplier name and catalog numbers for reagents used in flow cytometry study.

Residue	Chemical shifts: δ (ppm)			Secondary Chemical Shift: Δδ (ppm)		
	CO	Cα	Cβ	CO	Cα	Cβ
S	170.4	55.3	63.7	-2.5	-1.3	1.6

L	172.9	52.1	44.7	-3.0	-1.3	4.0

Table S4. Chemical Shift Assignments for carbons in S and L residues. Repeated S and L residues in K1 exhibit NMR chemical shifts consistent with β-strand secondary structure.(*23, 24*)

Supplementary Methods

Supplementary Methods 1: Detailed NMR Assignments

For ^{13}C CPMAS NMR Spectrum of K1, gaussian peak fitting was applied to extract chemical shifts (δ) corresponding specifically to the abundant S and L carbon sites from the ^{13}C CPMAS NMR spectrum of K1 (K-SLSLSLSLSLSL-K) peptide. These chemical shift assignments assume that signals from terminal lysine residues are minimal in comparison to those from repeated S and L residues. Secondary chemical shifts for S and L residues were calculated as $\Delta\delta = \delta_{sample} - \delta_{random\ coil}$, representing the deviation between chemical shifts of the carbons in the sample and shifts corresponding to the carbon if the sample were random coil.(*23*) In β-strand conformations, negative Δδ values are typically observed for the carbonyl (CO) and α-carbon (Cα) sites, whereas positive Δδ values are observed for β-carbon (Cβ) sites.(*23, 24*) Consistent with this β-strand signature, peptide K1 exhibits the expected Δδ pattern of – , – , + for CO, Cα, Cβ atoms. The measured secondary shifts for the CO, Cα, Cβ carbons in K1 are summarized in Table S4.

While the site-specific assignments on K1 are tentative as the terminal lysine aren't explicitly accounted for, these assignments coupled with the CD spectroscopy strongly supports the presence of β-strand secondary structure in K1. Moreover, as K1 and all molar ratios of K1 and SLan exhibit highly similar NMR spectra (**Figure 2b**) and display consistent β-strand signatures by CD spectroscopy (**Figure 2a**), we can conclude that all molar ratios of K1 and SLan adopt β-strand secondary structure.

Supplementary Methods 2: Detailed Molecular Modeling & Dynamics Methods

The generation of fibrils is performed using 3 .pml Pymol scripts to arrange 60-mer fibril representations of K1 in parallel, planar parallel, or antiparallel configurations. A sample script for the antiparallel configuration is below; all three scripts can be found as .pml files in the Supplementary Information.

```
#       Create Monomer 1
#
fab KSLSLSLSLSLSLK
orient
#
#       Create Monomer 2, flip orientation along z axis, move up 9 Angstroms
#
cmd.create(None,"obj01",zoom=0)
rotate z, 180, obj02
translate [0,9,0], obj02
#
#       Create Monomers 3 & 4, flip orientation along y-axis
#
cmd.create(None,"obj01",zoom=0)
cmd.create(None,"obj02",zoom=0)
rotate y, 180, obj03
rotate y, 180, obj04
#
#       Space along z-axis 5 Angstroms
#
translate [0,0,5], obj03
translate [0,0,5], obj04
```

```
#
#       Create and place monomers 5-8
#
cmd.create(None,"obj01",zoom=0)
cmd.create(None,"obj02",zoom=0)
cmd.create(None,"obj03",zoom=0)
cmd.create(None,"obj04",zoom=0)
translate [0,0,10], obj05
translate [0,0,10], obj06
translate [0,0,10], obj07
translate [0,0,10], obj08
#
#       Create and place monomers 9-12
#
cmd.create(None,"obj05",zoom=0)
cmd.create(None,"obj06",zoom=0)
cmd.create(None,"obj07",zoom=0)
cmd.create(None,"obj08",zoom=0)
translate [0,0,10], obj09
translate [0,0,10], obj10
translate [0,0,10], obj11
translate [0,0,10], obj12
#
#       Create and place monomers 13-16
#
cmd.create(None,"obj09",zoom=0)
cmd.create(None,"obj10",zoom=0)
cmd.create(None,"obj11",zoom=0)
cmd.create(None,"obj12",zoom=0)
translate [0,0,10], obj13
translate [0,0,10], obj14
translate [0,0,10], obj15
translate [0,0,10], obj16
#
#       Create and place monomers 17-20
#
cmd.create(None,"obj13",zoom=0)
cmd.create(None,"obj14",zoom=0)
cmd.create(None,"obj15",zoom=0)
cmd.create(None,"obj16",zoom=0)
translate [0,0,10], obj17
translate [0,0,10], obj18
translate [0,0,10], obj19
translate [0,0,10], obj20
#
#       Create and place monomers 21-24
#
cmd.create(None,"obj17",zoom=0)
cmd.create(None,"obj18",zoom=0)
cmd.create(None,"obj19",zoom=0)
cmd.create(None,"obj20",zoom=0)
```

```
translate [0,0,10], obj21
translate [0,0,10], obj22
translate [0,0,10], obj23
translate [0,0,10], obj24
#
#       Create and place monomers 25-28
#
cmd.create(None,"obj21",zoom=0)
cmd.create(None,"obj22",zoom=0)
cmd.create(None,"obj23",zoom=0)
cmd.create(None,"obj24",zoom=0)
translate [0,0,10], obj25
translate [0,0,10], obj26
translate [0,0,10], obj27
translate [0,0,10], obj28
#
#       Create and place monomers 29-32
#
cmd.create(None,"obj25",zoom=0)
cmd.create(None,"obj26",zoom=0)
cmd.create(None,"obj27",zoom=0)
cmd.create(None,"obj28",zoom=0)
translate [0,0,10], obj29
translate [0,0,10], obj30
translate [0,0,10], obj31
translate [0,0,10], obj32
#
#       Create and place monomers 33-36
#
cmd.create(None,"obj29",zoom=0)
cmd.create(None,"obj30",zoom=0)
cmd.create(None,"obj31",zoom=0)
cmd.create(None,"obj32",zoom=0)
translate [0,0,10], obj33
translate [0,0,10], obj34
translate [0,0,10], obj35
translate [0,0,10], obj36
#
#       Create and place monomers 37-40
#
cmd.create(None,"obj33",zoom=0)
cmd.create(None,"obj34",zoom=0)
cmd.create(None,"obj35",zoom=0)
cmd.create(None,"obj36",zoom=0)
translate [0,0,10], obj37
translate [0,0,10], obj38
translate [0,0,10], obj39
translate [0,0,10], obj40
#
#       Create and place monomers 41-44
#
```

```
cmd.create(None,"obj37",zoom=0)
cmd.create(None,"obj38",zoom=0)
cmd.create(None,"obj39",zoom=0)
cmd.create(None,"obj40",zoom=0)
translate [0,0,10], obj41
translate [0,0,10], obj42
translate [0,0,10], obj43
translate [0,0,10], obj44
#
#       Create and place monomers 45-48
#
cmd.create(None,"obj41",zoom=0)
cmd.create(None,"obj42",zoom=0)
cmd.create(None,"obj43",zoom=0)
cmd.create(None,"obj44",zoom=0)
translate [0,0,10], obj45
translate [0,0,10], obj46
translate [0,0,10], obj47
translate [0,0,10], obj48
#
#       Create and place monomers 49-52
#
cmd.create(None,"obj45",zoom=0)
cmd.create(None,"obj46",zoom=0)
cmd.create(None,"obj47",zoom=0)
cmd.create(None,"obj48",zoom=0)
translate [0,0,10], obj49
translate [0,0,10], obj50
translate [0,0,10], obj51
translate [0,0,10], obj52
#
#       Create and place monomers 53-56
#
cmd.create(None,"obj49",zoom=0)
cmd.create(None,"obj50",zoom=0)
cmd.create(None,"obj51",zoom=0)
cmd.create(None,"obj52",zoom=0)
translate [0,0,10], obj53
translate [0,0,10], obj54
translate [0,0,10], obj55
translate [0,0,10], obj56
#
#       Create and place monomers 57-60
#
cmd.create(None,"obj53",zoom=0)
cmd.create(None,"obj54",zoom=0)
cmd.create(None,"obj55",zoom=0)
cmd.create(None,"obj56",zoom=0)
translate [0,0,10], obj57
translate [0,0,10], obj58
translate [0,0,10], obj59
```

```
translate [0,0,10], obj60

#
#          Assign a chain and segi value for each monomer
#
alter obj01, chain='A'
alter obj02, chain='B'
alter obj03, chain='C'
alter obj04, chain='D'
alter obj05, chain='E'
alter obj06, chain='F'
alter obj07, chain='G'
alter obj08, chain='H'
alter obj09, chain='I'
alter obj10, chain='J'
alter obj11, chain='K'
alter obj12, chain='L'
alter obj13, chain='M'
alter obj14, chain='N'
alter obj15, chain='O'
alter obj16, chain='P'
alter obj17, chain='Q'
alter obj18, chain='R'
alter obj19, chain='S'
alter obj20, chain='T'
#
alter obj21, chain='A'
alter obj22, chain='B'
alter obj23, chain='C'
alter obj24, chain='D'
alter obj25, chain='E'
alter obj26, chain='F'
alter obj27, chain='G'
alter obj28, chain='H'
alter obj29, chain='I'
alter obj30, chain='J'
alter obj31, chain='K'
alter obj32, chain='L'
alter obj33, chain='M'
alter obj34, chain='N'
alter obj35, chain='O'
alter obj36, chain='P'
alter obj37, chain='Q'
alter obj38, chain='R'
alter obj39, chain='S'
alter obj40, chain='T'
#
alter obj41, chain='A'
alter obj42, chain='B'
alter obj43, chain='C'
alter obj44, chain='D'
```

```
alter obj45, chain='E'
alter obj46, chain='F'
alter obj47, chain='G'
alter obj48, chain='H'
alter obj49, chain='I'
alter obj50, chain='J'
alter obj51, chain='K'
alter obj52, chain='L'
alter obj53, chain='M'
alter obj54, chain='N'
alter obj55, chain='O'
alter obj56, chain='P'
alter obj57, chain='Q'
alter obj58, chain='R'
alter obj59, chain='S'
alter obj60, chain='T'
#
alter obj01, segi='A'
alter obj02, segi='A'
alter obj03, segi='A'
alter obj04, segi='A'
alter obj05, segi='A'
alter obj06, segi='A'
alter obj07, segi='A'
alter obj08, segi='A'
alter obj09, segi='A'
alter obj10, segi='A'
alter obj11, segi='A'
alter obj12, segi='A'
alter obj13, segi='A'
alter obj14, segi='A'
alter obj15, segi='A'
alter obj16, segi='A'
alter obj17, segi='A'
alter obj18, segi='A'
alter obj19, segi='A'
alter obj20, segi='A'
#
#
alter obj21, segi='B'
alter obj22, segi='B'
alter obj23, segi='B'
alter obj24, segi='B'
alter obj25, segi='B'
alter obj26, segi='B'
alter obj27, segi='B'
alter obj28, segi='B'
alter obj29, segi='B'
alter obj30, segi='B'
alter obj31, segi='B'
alter obj32, segi='B'
```

```
alter obj33, segi='B'
alter obj34, segi='B'
alter obj35, segi='B'
alter obj36, segi='B'
alter obj37, segi='B'
alter obj38, segi='B'
alter obj39, segi='B'
alter obj40, segi='B'
#
alter obj41, segi='C'
alter obj42, segi='C'
alter obj43, segi='C'
alter obj44, segi='C'
alter obj45, segi='C'
alter obj46, segi='C'
alter obj47, segi='C'
alter obj48, segi='C'
alter obj49, segi='C'
alter obj50, segi='C'
alter obj51, segi='C'
alter obj52, segi='C'
alter obj53, segi='C'
alter obj54, segi='C'
alter obj55, segi='C'
alter obj56, segi='C'
alter obj57, segi='C'
alter obj58, segi='C'
alter obj59, segi='C'
alter obj60, segi='C'
```

To make the combination fibrils, a representation of SLan (generated outside of Pymol) was aligned to the Excel designated positions using Pymol's align tools. Alternatively, to randomize the distribution of subunits in the SLan-K1 60mer assemblies, a TCL script was developed to randomly place the specified variants across the 60 possible positions. Both sets of scripts are available in the following Zenodo repository: https://doi.org/10.5281/zenodo.19742094

The cutoffs of van der Waals (vdW) and Coulombic coupling were 10 Å. The particle mesh Ewald (PME) method was used for the evaluation of long-range Coulombic interactions and to increase the efficiency of the simulations. (*58*)The simulations were performed in the NPT ensemble (P = 1 bar and T = 310 K). The systems were simulated for 200 ns using the Langevin dynamics with a damping constant of 1 ps^{-1} and a time step of 2 fs and repeated 3 times to ensure consistency for initial configuration-dependent structures.(*59*). The self-assembly of the fiber was simulated for 1 microsecond. The trajectories were analyzed using the NAMD energy plugin by using the last 20 ns of simulations.

The electrostatic and Van der Waals energetic contributions between the interacting residues were calculated by the NAMD energy plugin for atoms within a 10 Å. The electrostatic contribution is given by Equation (1):

$$U_{elec} = \sum_{i=1}^{n} \sum_{j=1}^{n} \frac{1}{4\pi\varepsilon} \frac{q_i q_j}{|\vec{r_i} - \vec{r_j}|} \quad (1)$$

Where ε is the dielectric constant of the water, q_i and q_j are two distinct charges, $\vec{r}_i$ is the vector position of charge q_i, and $\vec{r}_j$ is the distance between the two charges q_i and q_j. To increase the efficiency of the simulations, pairwise interaction calculations were not performed beyond a maximum cutoff distance (10 Å). Long-range electrostatic interactions were calculated by the PME. (*60, 61*)

The Lennard-Jones (LJ) 6–12 potential energy equation was used to calculate the magnitude of the Van der Waals interactions and close distance atomic repulsions, given by Equation (2):

$$U_{LJ} = \sum_{i=1}^{n} \sum_{j>i}^{n} \varepsilon_{ij} \left[\left(\frac{\sigma_{ij}}{r_{ij}} \right)^{12} - \left(\frac{\sigma_{ij}}{r_{ij}} \right)^{6} \right] \quad (2)$$

REFERENCES

1. B. R. Freedman, C. Hwang, S. Talbot, B. Hibler, S. Matoori, D. J. Mooney, Breakthrough treatments for accelerated wound healing. *Sci. Adv.* **9**, eade7007 (2023).

2. M. Chang, T. T. Nguyen, Strategy for treatment of infected diabetic foot ulcers. *Acc. Chem. Res.* **54**, 1080–1093 (2021).

3. N. Papanas, E. Maltezos, Becaplermin gel in the treatment of diabetic neuropathic foot ulcers. *Clin. Interv. Aging* **3**, 233–240 (2008).

4. Y. Xue, Y. Zhang, Y. Zhong, S. Du, X. Hou, W. Li, H. Li, S. Wang, C. Wang, J. Yan, D. D. Kang, B. Deng, D. W. McComb, D. J. Irvine, R. Weiss, Y. Dong, LNP-RNA-engineered adipose stem cells for accelerated diabetic wound healing. *Nat. Commun.* **15**, 739 (2024).

5. J. Hu, L. Zhang, C. Liechty, C. Zgheib, M. M. Hodges, K. W. Liechty, J. Xu, Long noncoding RNA GAS5 regulates macrophage polarization and diabetic wound healing. *J. Invest. Dermatol.* **140**, 1629–1638 (2020).

6. X. Li, N. Li, B. Li, Y. Feng, D. Zhou, G. Chen, Noncoding RNAs and RNA-binding proteins in diabetic wound healing. *Bioorg. Med. Chem. Lett.* **50**, 128311 (2021).

7. Y. Zhang, Y.-Y. Zhang, Z.-W. Pan, Q.-Q. Li, L.-H. Sun, X. Li, M.-Y. Gong, X.-W. Yang, Y.-Y. Wang, H.-D. Li, L.-N. Xuan, Y.-C. Shao, M.-M. Li, M.-Y. Zhang, Q. Yu, Z. Li, X.-F. Zhang, D.-H. Liu, Y.-M. Zhu, Z.-Y. Tan, Y.-Y.

Zhang, Y.-Q. Liu, Y. Zhang, L. Jiao, B.-F. Yang, GDF11 promotes wound healing in diabetic mice via stimulating HIF-1α-VEGF/SDF-1α-mediated endothelial progenitor cell mobilization and neovascularization. *Acta Pharmacol. Sin.* **44**, 999–1013 (2023).

8. V. A. Kumar, N. L. Taylor, S. Shi, B. K. Wang, A. A. Jalan, M. K. Kang, N. C. Wickremasinghe, J. D. Hartgerink, Highly angiogenic peptide nanofibers. *ACS Nano* **9**, 860–868 (2015).

9. L. D. D'Andrea, G. Iaccarino, R. Fattorusso, D. Sorriento, C. Carannante, D. Capasso, B. Trimarco, C. Pedone, Targeting angiogenesis: Structural characterization and biological properties of a de novo engineered VEGF mimicking peptide. *Proc. Natl. Acad. Sci. U.S.A.* **102**, 14215–14220 (2005).

10. V. A. Kumar, Q. Liu, N. C. Wickremasinghe, S. Shi, T. T. Cornwright, Y. Deng, A. Azares, A. N. Moore, A. M. Acevedo-Jake, N. R. Agudo, S. Pan, D. G. Woodside, P. Vanderslice, J. T. Willerson, R. A. Dixon, J. D. Hartgerink, Treatment of hind limb ischemia using angiogenic peptide nanofibers. *Biomaterials* **98**, 113–119 (2016).

11. K. M. Galler, L. Aulisa, K. R. Regan, R. N. D'Souza, J. D. Hartgerink, Self-assembling multidomain peptide hydrogels: Designed susceptibility to enzymatic cleavage allows enhanced cell migration and spreading. *J. Am. Chem. Soc.* **132**, 3217–3223 (2010).

12. L. Aulisa, H. Dong, J. D. Hartgerink, Self-assembly of multidomain peptides: Sequence variation allows control over cross-linking and viscoelasticity. *Biomacromolecules* **10**, 2694–2698 (2009).

13. Z. Siddiqui, B. Sarkar, K. K. Kim, N. Kadincesme, R. Paul, A. Kumar, Y. Kobayashi, A. Roy, M. Choudhury, J. Yang, E. Shimizu, V. A. Kumar, Angiogenic hydrogels for dental pulp revascularization. *Acta Biomater.* **126**, 109–118 (2021).

14. J. Dodd-O, A. Roy, Z. Siddiqui, R. Jafari, F. Coppola, S. Ramasamy, A. Kolloli, D. Kumar, S. Kaundal, B. Zhao, R. Kumar, A. S. Robang, J. Li, A.-R. Azizogli, V. Pai, A. Acevedo-Jake, C. Heffernan, A. Lucas, A. C. McShan, A. K. Paravastu, B. V. V. Prasad, S. Subbian, P. Král, V. Kumar, Antiviral fibrils of self-assembled peptides with tunable compositions. *Nat. Commun.* **15**, 1142 (2024).

15. M. J. Webber, J. Tongers, C. J. Newcomb, K. T. Marquardt, J. Bauersachs, D. W. Losordo, S. I. Stupp, Supramolecular nanostructures that mimic VEGF as a strategy for ischemic tissue repair. *Proc. Natl. Acad. Sci. U.S.A.* **108**, 13438–13443 (2011).

16. A. N. Moore, T. L. Lopez Silva, N. C. Carrejo, C. A. Origel Marmolejo, I. C. Li, J. D. Hartgerink, Nanofibrous peptide hydrogel elicits angiogenesis and neurogenesis without drugs, proteins, or cells. *Biomaterials* **161**, 154–163 (2018).

17. L.-C. Huang, H.-C. Wang, L.-H. Chen, C.-Y. Ho, P.-H. Hsieh, M.-Y. Huang, H. C. Wu, T. W. Wang, Bioinspired self-assembling peptide hydrogel with proteoglycan-assisted growth factor delivery for therapeutic angiogenesis. *Theranostics* **9**, 7072–7087 (2019).

18. N. C. Wickremasinghe, V. A. Kumar, S. Shi, J. D. Hartgerink, Controlled angiogenesis in peptide nanofiber composite hydrogels. *ACS Biomater. Sci. Eng.* **1**, 845–854 (2015).

19. C. Han, Z. Zhang, J. Sun, K. Li, Y. Li, C. Ren, Q. Meng, J. Yang, Self-assembling peptide-based hydrogels in angiogenesis. *Int. J. Nanomedicine* **15**, 10257–10269 (2020).

20. A. S. Robang, A. Roy, J. B. Dodd-O, D. He, J. V. Le, A. C. McShan, Y. Hu, V. A. Kumar, A. K. Paravastu, Structural consequences of introducing bioactive domains to designer β-sheet peptide self-assemblies. *Biomacromolecules* **25**, 1429–1438 (2024).

21. A. Roy, J. B. Dodd-O, A. S. Robang, D. He, O. West, Z. Siddiqui, E. D. Aguas, H. Goldberg, A. Griffith, C. Heffernan, Y. Hu, A. K. Paravastu, V. A. Kumar, Self-assembling peptides with insulin-like growth factor mimicry. *ACS Appl. Mater. Interfaces* **16**, 364–375 (2024).

22. E. O. Stejskal, J. Schaefer, J. S. Waugh, Magic-angle spinning and polarization transfer in proton-enhanced NMR. *J. Magn. Reson.* **28**, 105–112 (1977).

23. P. R. Romero, N. Kobayashi, J. R. Wedell, K. Baskaran, T. Iwata, M. Yokochi, D. Maziuk, H. Yao, T. Fujiwara, G. Kurusu, E. L. Ulrich, J. C. Hoch, J. L. Markley, BioMagResBank (BMRB) as a resource for structural biology. *Methods Mol. Biol.* **2112**, 187–218 (2020).

24. D. S. Wishart, B. D. Sykes, F. M. Richards, The chemical shift index: A fast and simple method for the assignment of protein secondary structure through NMR spectroscopy. *Biochemistry* **31**, 1647–1651 (1992).

25. V. Daebel, S. Chinnathambi, J. Biernat, M. Schwalbe, B. Habenstein, A. Loquet, E. Akoury, K. Tepper, H. Müller, M. Baldus, C. Griesinger, M. Zweckstetter, E. Mandelkow, V. Vijayan, A. Lange, β-Sheet core of tau paired helical filaments revealed by solid-state NMR. *J. Am. Chem. Soc.* **134**, 13982–13989 (2012).

26. G. T. Debelouchina, G. W. Platt, M. J. Bayro, S. E. Radford, R. G. Griffin, Magic angle spinning nmr analysis of β2-microglobulin amyloid fibrils in two distinct morphologies. *J. Am. Chem. Soc.* **132**, 10414–10423 (2010).

27. M. Sarker, S. Park, V. Kumar, C. H. Lee, Micro-thin hydrogel coating integrated in 3D printing for spatiotemporal delivery of bioactive small molecules. *Biofabrication* **17**, 015019 (2024).

28. B. Sarkar, X. Ma, A. Agas, Z. Siddiqui, P. Iglesias-Montoro, P. K. Nguyen, K. K. Kim, J. Haorah, V. A. Kumar, In vivo neuroprotective effect of a self-assembled peptide hydrogel. *Chem. Eng. J.* **408**, 127295 (2021).

29. V. Harbour, C. Casillas, Z. Siddiqui, B. Sarkar, S. Sanyal, P. Nguyen, K. K. Kim, A. Roy, P. Iglesias-Montoro, S. Patel, F. Podlaski, P. Tolias, W. Windsor, V. Kumar, Regulation of lipoprotein homeostasis by self-assembling peptides. *ACS Appl. Bio Mater.* **3**, 8978–8988 (2020).

30. P. K. Nguyen, B. Sarkar, Z. Siddiqui, M. McGowan, P. Iglesias-Montoro, S. Rachapudi, S. Kim, W. Gao, E. J. Lee, V. A. Kumar, Self-assembly of an antiangiogenic nanofibrous peptide hydrogel. *ACS Appl. Bio Mater.* **1**, 865–870 (2018).

31. K. K. Kim, Z. Siddiqui, M. Patel, B. Sarkar, V. A. Kumar, A self-assembled peptide hydrogel for cytokine sequestration. *J. Mater. Chem. B* **8**, 945–950 (2020).

32. B. Sarkar, Z. Siddiqui, P. K. Nguyen, N. Dube, W. Fu, S. Park, S. Jaisinghani, R. Paul, S. D. Kozuch, D. Deng, P. Iglesias-Montoro, M. Li, D. Sabatino, D. S. Perlin, W. Zhang, J. Mondal, V. A. Kumar, Membrane-disrupting nanofibrous peptide hydrogels. *ACS Biomater. Sci. Eng.* **5**, 4657–4670 (2019).

33. P. K. Nguyen, W. Gao, S. D. Patel, Z. Siddiqui, S. Weiner, E. Shimizu, B. Sarkar, V. A. Kumar, Self-assembly of a dentinogenic peptide hydrogel. *ACS Omega* **3**, 5980–5987 (2018).

34. K. Kim, Z. Siddiqui, A. M. Acevedo-Jake, A. Roy, M. Choudhury, J. Grasman, V. Kumar, Angiogenic hydrogels to accelerate early wound healing. *Macromol. Biosci.* **22**, e2200067 (2022).

35. B. Sarkar, P. K. Nguyen, W. Gao, A. Dondapati, Z. Siddiqui, V. A. Kumar, Angiogenic self-assembling peptide scaffolds for functional tissue regeneration. *Biomacromolecules* **19**, 3597–3611 (2018).

36. A. N. Moore, J. D. Hartgerink, Self-assembling multidomain peptide nanofibers for delivery of bioactive molecules and tissue regeneration. *Acc. Chem. Res.* **50**, 714–722 (2017).

37. Z. Álvarez, A. N. Kolberg-Edelbrock, I. R. Sasselli, J. A. Ortega, R. Qiu, Z. Syrgiannis, P. A. Mirau, F. Chen, S. M. Chin, S. Weigand, E. Kiskinis, S. I. Stupp, Bioactive scaffolds with enhanced supramolecular motion promote recovery from spinal cord injury. *Science* **374**, 848–856 (2021).

38. X. Ma, A. Agas, Z. Siddiqui, K. Kim, P. Iglesias-Montoro, J. Kalluru, V. Kumar, J. Haorah, Angiogenic peptide hydrogels for treatment of traumatic brain injury. *Bioact. Mater.* **5**, 124–132 (2020).

39. D. Grant, N. Wanner, M. Frimel, S. Erzurum, K. Asosingh, Comprehensive phenotyping of endothelial cells using flow cytometry 1: Murine. *Cytometry A* **99**, 251–256 (2021).

40. D. Toledo-Flores, A. Williamson, N. Schwarz, S. Fernando, C. Dimasi, T. A. Witt, T. M. Nguyen, A. S. Puranik, C. D. Chue, S. Delacroix, D. B. Spoon, C. S. Bonder, C. A. Bursill, B. A. Di Bartolo, S. J. Nicholls, R. D. Simari, P. J. Psaltis, Vasculogenic properties of adventitial Sca-1^{+}CD45^{+} progenitor cells in mice: A potential source of vasa vasorum in atherosclerosis. *Sci. Rep.* **9**, 7286 (2019).

41. T. L. Lopez-Silva, C. F. Anderson, J. P. Schneider, Modulating neutrophil extracellular trap formation in vivo with locoregional precision using differently charged self-assembled hydrogels. *ACS Cent. Sci.* **11**, 465–478 (2025).

42. A. Hernandez, J. D. Hartgerink, S. Young, Self-assembling peptides as immunomodulatory biomaterials. *Front. Bioeng. Biotechnol.* **11**, 1139782 (2023).

43. M. A. Fernandez-Yague, L. A. Hymel, C. E. Olingy, C. McClain, M. E. Ogle, J. R. García, D. Minshew, S. Vyshnya, H. S. Lim, P. Qiu, A. J. García, E. A. Botchwey, Analyzing immune response to engineered hydrogels by hierarchical clustering of inflammatory cell subsets. *Sci. Adv.* **8**, eabd8056 (2022).

44. F. Veglia, E. Sanseviero, D. I. Gabrilovich, Myeloid-derived suppressor cells in the era of increasing myeloid cell diversity. *Nat. Rev. Immunol.* **21**, 485–498 (2021).

45. V. Bronte, S. Brandau, S. H. Chen, M. P. Colombo, A. B. Frey, T. F. Greten, S. Mandruzzato, P. J. Murray, A. Ochoa, S. Ostrand-Rosenberg, P. C. Rodriguez, A. Sica, V. Umansky, R. H. Vonderheide, D. I. Gabrilovich, Recommendations for myeloid-derived suppressor cell nomenclature and characterization standards. *Nat. Commun.* **7**, 12150 (2016).

46. B. H. Pogostin, M. H. Yu, A. R. Azares, E. M. Euliano, C. S. E. Lai, G. Saenz, S. X. Wu, A. C. Farsheed, S. M. Melhorn, T. P. Graf, D. G. Woodside,

J. D. Hartgerink, K. J. McHugh, Multidomain peptide hydrogel adjuvants elicit strong bias towards humoral immunity. *Biomater. Sci.* **10**, 6217–6229 (2022).

47. A. Cossarizza, H.-D. Chang, A. Radbruch, S. Abrignani, R. Addo, M. Akdis, I. Andrä, F. Andreata, F. Annunziato, E. Arranz, P. Bacher, S. Bari, V. Barnaba, J. Barros-Martins, D. Baumjohann, C. G. Beccaria, D. Bernardo, D. A. Boardman, J. Borger, C. Böttcher, L. Brockmann, M. Burns, D. H. Busch, G. Cameron, I. Cammarata, A. Cassotta, Y. Chang, F. G. Chirdo, E. Christakou, L. Čičin-Šain, L. Cook, A. J. Corbett, R. Cornelis, L. Cosmi, M. S. Davey, S. De Biasi, G. De Simone, G. D. Zotto, M. Delacher, F. D. Rosa, J. D. Santo, A. Diefenbach, J. Dong, T. Dörner, R. J. Dress, C.-A. Dutertre, S. B. G. Eckle, P. Eede, M. Evrard, C. S. Falk, M. Feuerer, S. Fillatreau, A. Fiz-Lopez, M. Follo, G. A. Foulds, J. Fröbel, N. Gagliani, G. Galletti, A. Gangaev, N. Garbi, J. A. Garrote, J. Geginat, N. A. Gherardin, L. Gibellini, F. Ginhoux, D. I. Godfrey, P. Gruarin, C. Haftmann, L. Hansmann, C. M. Harpur, A. C. Hayday, G. Heine, D. C. Hernández, M. Herrmann, O. Hoelsken, Q. Huang, S. Huber, J. E. Huber, J. Huehn, M. Hundemer, W. Y. K. Hwang, M. Iannacone, S. M. Ivison, H.-M. Jäck, P. K. Jani, B. Keller, N. Kessler, S. Ketelaars, L. Knop, J. Knopf, H.-F. Koay, K. Kobow, K. Kriegsmann, H. Kristyanto, A. Krueger, J. F. Kuehne, H. Kunze-Schumacher, P. Kvistborg, I. Kwok, D. Latorre, D. Lenz, M. K. Levings, A. C. Lino, F. Liotta, H. M. Long, E. Lugli, K. N. Mac Donald, L. Maggi, M. K. Maini, F. Mair, C. Manta, R. A. Manz, M.-F. Mashreghi, A. Mazzoni, J. M. Cluskey, H. E. Mei, F. Melchers, S. Melzer, D. Mielenz, L. Monin, L. Moretta, G. Multhoff, L. E. Muñoz, M. Muñoz-Ruiz, F. Muscate, A. Natalini, K. Neumann, L. G. Ng, A. Niedobitek, J. Niemz, L. N. Almeida, S.

Notarbartolo, L. Ostendorf, L. J. Pallett, A. A. Patel, G. I. Percin, G. Peruzzi, M. Pinti, A. G. Pockley, K. Pracht, I. Prinz, I. Pujol-Autonell, N. Pulvirenti, L. Quatrini, K. M. Quinn, H. Radbruch, H. Rhys, M. B. Rodrigo, C. Romagnani, C. Saggau, S. Sakaguchi, F. Sallusto, L. Sanderink, I. Sandrock, C. Schauer, A. Scheffold, H. U. Scherer, M. Schiemann, F. A. Schildberg, K. Schober, J. Schoen, W. Schuh, T. Schüler, A. R. Schulz, S. Schulz, J. Schulze, S. Simonetti, J. Singh, K. M. Sitnik, R. Stark, S. Starossom, C. Stehle, F. Szelinski, L. Tan, A. Tarnok, J. Tornack, T. I. M. Tree, J. J. P. van Beek, W. van de Veen, K. van Gisbergen, C. Vasco, N. A. Verheyden, A. von Borstel, K. A. Ward-Hartstonge, K. Warnatz, C. Waskow, A. Wiedemann, A. Wilharm, J. Wing, O. Wirz, J. Wittner, J. H. M. Yang, J. Yang, Guidelines for the use of flow cytometry and cell sorting in immunological studies (third edition). *Eur. J. Immunol.* **51**, 2708–3145 (2021).

48. M. H. Sangji, S. R. Lee, H. Sai, S. Weigand, L. C. Palmer, S. I. Stupp, Self-sorting vs coassembly in peptide amphiphile supramolecular nanostructures. *ACS Nano* **18**, 15878–15887 (2024).

49. C. R. Morcombe, K. W. Zilm, Chemical shift referencing in MAS solid state NMR. *J. Magn. Reson.* **162**, 479–486 (2003).

50. J. Huang, A. D. MacKerell Jr., CHARMM36 all-atom additive protein force field: Validation based on comparison to NMR data. *J. Comput. Chem.* **34**, 2135–2145 (2013).

51. K. Vanommeslaeghe, E. Hatcher, C. Acharya, S. Kundu, S. Zhong, J. Shim, E. Darian, O. Guvench, P. Lopes, I. Vorobyov, A. D. Mackerell Jr., CHARMM general force field: A force field for drug-like molecules compatible with the CHARMM all-atom additive biological force fields. *J. Comput. Chem.* **31**, 671–690 (2010).

52. J. C. Phillips, D. J. Hardy, J. D. C. Maia, J. E. Stone, J. V. Ribeiro, R. C. Bernardi, R. Buch, G. Fiorin, J. Hénin, W. Jiang, R. McGreevy, M. C. R. Melo, B. K. Radak, R. D. Skeel, A. Singharoy, Y. Wang, B. Roux, A. Aksimentiev, Z. Luthey-Schulten, L. V. Kalé, K. Schulten, C. Chipot, E. Tajkhorshid, Scalable molecular dynamics on CPU and GPU architectures with NAMD. *J. Chem. Phys.* **153**, 044130 (2020).

53. K. M. Crowe, Z. Siddiqui, V. Harbour, K. Kim, S. Syed, R. Paul, A. Roy, R. Naik, K. Mitchell, A. Mahajan, B. Sarkar, V. A. Kumar, Evaluation of injectable naloxone-releasing hydrogels. *ACS Appl. Bio Mater.* **3**, 7858–7864 (2020).

54. M. Jerabek-Willemsen, C. J. Wienken, D. Braun, P. Baaske, S. Duhr, Molecular interaction studies using microscale thermophoresis. *Assay Drug Dev. Technol.* **9**, 342–353 (2011).

55. A. Langer, T. Bartoschik, O. Cehlar, S. Duhr, P. Baaske, W. Streicher, A new spectral shift-based method to characterize molecular interactions. *Assay Drug Dev. Technol.* **20**, 83–94 (2022).

56. M. J. Chen, S. Ramesha, L. D. Weinstock, T. Gao, L. Ping, H. Xiao, E. B. Dammer, D. D. Duong, A. I. Levey, J. J. Lah, N. T. Seyfried, L. B. Wood, S.

Rangaraju, Extracellular signal-regulated kinase regulates microglial immune responses in Alzheimer's disease. *J. Neurosci. Res.* **99**, 1704–1721 (2021).

57. T. L. Lopez-Silva, D. G. Leach, A. Azares, I. C. Li, D. G. Woodside, J. D. Hartgerink, Chemical functionality of multidomain peptide hydrogels governs early host immune response. *Biomaterials* **231**, 119667 (2020).

58. T. Darden, D. York, L. Pedersen, Particle mesh Ewald: An N·log(N) method for Ewald sums in large systems. *J. Chem. Phys.* **98**, 10089–10092 (1993).

59. Y. Han, P. Král, Computational design of ACE2-based peptide inhibitors of SARS-CoV-2. *ACS Nano* **14**, 5143–5147 (2020).

60. F. Coppola, T. Pavlíček, P. Král, Coupling of SARS-CoV-2 to Aβ amyloid fibrils. *ACS Omega* **9**, 9295–9299 (2024).

61. A. R. Azizogli, V. Pai, F. Coppola, R. Jafari, J. B. Dodd-O, R. Harish, B. Balasubramanian, J. Kashyap, A. M. Acevedo-Jake, P. Král, V. A. Kumar, Scalable inhibitors of the Nsp3-Nsp4 coupling in SARS-CoV-2. *ACS Omega* **8**, 5349–5360 (2023).